THE DRAGON
Recoil Separator
Optics

The Recoil Group

January 3, 2001

Contents

List of Figures

List of Tables

Chapter 1

Component description

1.1 Introduction

The following document describes the ion optics of the DRAGON electromagnetic separator. This is the most recent version of the document, in which effective lengths and fringing fields have been derived from measured field maps.

The design consists of a two stage mass separator that has been optimized to cleanly separate the much more intense beam from the recoiling product of radiative capture reactions. Clean separation is assured by first selecting a single charge state with a magnetic bender and by limiting the mass resolving power so that beam of the reactions of interest does not approach material surfaces too closely. In particular, the first stage has been designed to allow the ^{15}O beam of the reaction $^{15}\mathrm{O}(\alpha,\gamma)^{19}\mathrm{Ne}$, thought to be one of the key breakout reactions, to pass at a safe distance from the anode of the first electrostatic bender.

1.2 Component parameters

A top view of the DRAGON separator is shown in figure 1.1. The status of the field components as of the writing of this document is outlined below. For dipoles the important design parameters, listed in table 1.1, are the bending radii(ρ) and angles(ϕ), the inclination of the effective field boundaries at the entrance(α) and exit(β)($\alpha = \beta$ for MD1 and MD2), the pole gaps for the magnetic dipoles and the electrode gap for the electric dipoles(ED1 and ED2). The important design parameters, listed in table 1.2, are for quads(Q1 to Q10) and sextupoles (S1 to S4), the full aperture size, maximum field strengths (i.e. at pole tips for Q's and S's and central for SM's) and the effective(L_{eff}) and physical lengths(L_{tot}). Also shown in figure 1.1 are the X and Y steering magnets that will be used to correct for small misalignments of the components (see chapter that follows).

For the dipoles, due to the finite extent in z of the fringing field regions, there are shifts in x between the optical axes in the field free regions on either side and the

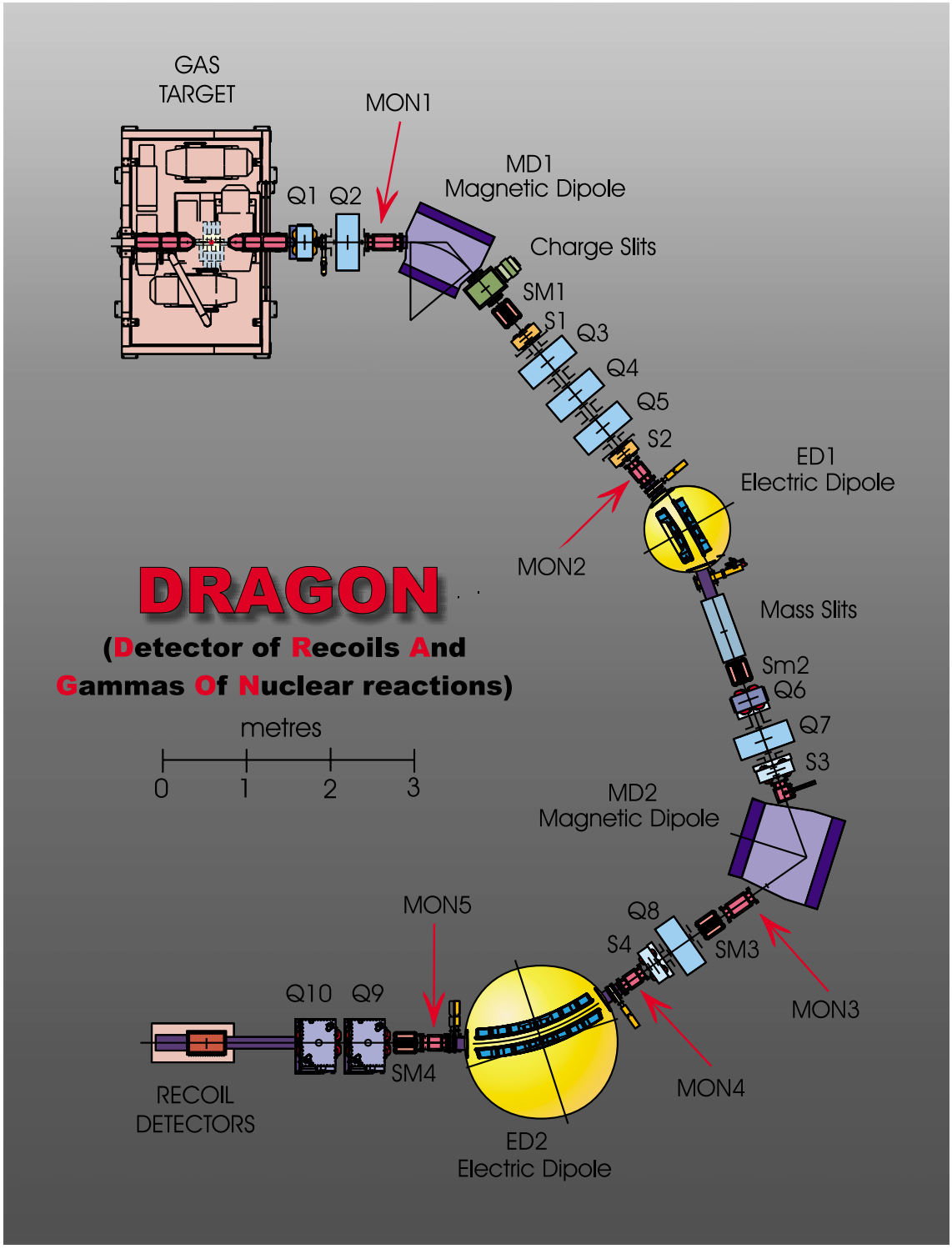

Figure 1.1: Top view of the DRAGON layout showing components of interest.

Table 1.1: Important parameters of DRAGON dipoles.

dipole	ρ(cm)	ϕ(deg)	α(deg)	gap(cm)	L_{eff}(cm)
MD_1	100	50	5.8	10	87.27
ED_1	200	20	-	10	69.81
MD_2	81.3	75	29	12	106.42
ED_2	250	35	-	10	152.72

Table 1.2: Important parameters and status of DRAGON quads(Q), sextupoles(S) and steering magnets(SM).

device	L_{eff}(cm)	L_{tot}(cm)	aperture(inch)	status
$Q_{1,6}$	25.23	31.5	4.25	mapped/placed
Q_2	33.385	45(?)	6.25	mapped/placed
$Q_{9,10}$	46.7	58.2	5.91	SMIT-ELMA quads mapped
$Q_{3..5,7,8}$	33.38	45(?)	6.25	mapped/placed
$S_{1,2}$	18.75	21.6	6.26	mapped
$S_{3,4}$	19.9	23.5	6.26(4.49) X(Y)	mapped asymmetric design
$SM_{3,4}$	25.9(?)	16.3	6.25	mapped(?)
$SM_{1,2}$	25.6	16.5	4.25	Chalk River mapped(rough)

circular optical axes in the uniform field regions. The sense of the shifts are towards the bending centres. These shifts are calculated by RAYTRACE using the latest estimates for the fringing fields (see ENGE coefficients describing these in the RAYTRACE input file in the appendix). Using them has the effect of displacing the circular trajectory symmetrically with respect to the pole face edges (for MD's) or electrodes (for ED's). For the magnetic dipoles we have ignored these shifts, placing alignment pins in the unshifted locations. In practice this is dealt with by reducing the field strengths of MD1 and MD2 from the RAYTRACE values to bring the optical axes downstream back to the desired direction. However, although these shifts shown in Table 1.3 are small, using them will make optimal use of the limited space between the electrodes of ED1 and ED2.

Table 1.3: Shifts in x, between the optical axes in the field free regions and the circular trajectories in the uniform field regions.

Dipole	Shift in x (mm)
MD1	-1.91
ED1	-.657
MD2	-3.32
ED2	-.89

Chapter 2

E.M. separator design and detailed specifications

This section describes a design of the separator which will meet the performance requirements subject to the constraints. The general "physics" requirements are translated into tolerances for construction of the hardware elements of the separator.

2.1 Ion optics design

The electromagnetic separator is composed of two stages, each one an independent mass separator containing a magnetic and an electric dipole plus focussing quadrupoles and aberration-correcting sextupoles. The design was carried out to third order with the GIOS optimization program, which uses Taylor expansions about a central trajectory to describe transport of ions from one point to another in the separator.

Electromagnetic elements (dipoles, quadrupoles, sextupoles,...) are described in first order by elements having a uniform field strength over an "effective length". The "central ray" (and the coordinate system of GIOS or RAYTRACE) consists of a sequence of straight-line segments containing drift lengths, quadrupoles, sextupoles, etc. connected to arcs of constant radius for each of the dipoles. Fringe-field effects appear in higher order calculations. Viewing downstream (the direction of particle motion) in a segment, positive values of the 'x' coordinate are to the left of the optic axis, positive values of 'y' are upward from the axis, and 'z' increases in the direction of particle motion. The magnetic multipole components are defined to be positive if $B_y > 0$ for x>0, y=0. Thus, for positively charged ions, a positive dipole field deflects ions to the right, a positive quadrupole field focuses horizontally and defocuses vertically, a positive sextupole field deflects ions in the y=0 plane to the right, etc. The multipole field strengths are the "pole-tip fields" — i.e. the radial component of field at the tip of a pole (the nominal aperture radius).

The layout of the separator is defined by extension of the straight-line segments until they meet; the lengths of the lines and the angles between them define the "backbone" for surveying. Table 2.1, Table 2.2, Table 2.3, Table 2.4 and Table 2.5 describe the

sizes, separations, and field strengths of the elements in the separator. Note that S0 in Table 2.5 refers to the pole tip sextupolar field used in the ion optical codes.

Table 2.1: First-order optics properties of magnetic and electrostatic dipoles (file reso2000.dat 28 Sept 00).

Element	Radius (m)	Bend (deg)	Direction	Gap (m)	Entry pole angle (deg)	Exit pole angle (deg)
MD1	1.00	50	Right	0.10	5.8	5.8
ED1	2.00	20	Right	0.10	0.0	0.0
MD2	0.813	75	Right	0.12	29.0	29.0
ED2	2.50	35	Right	0.10	0.0	0.0

Table 2.2: Separator backbone segment lengths (GIOS output file reso2000.dat 28 Sept 00).

Segment	Begins	Ends	Length (m)
1	Target	MD1	3.0163
2	MD1	ED1	4.7819
3	ED1	MD2	4.4815
4	MD2	ED2	4.1351
5	ED2	Final focus	4.2975
All	Target	Final focus	10.2461 (90.346°)

Table 2.3: E.M.S. element spacings in the first stage (file reso2000.dat 28 Sept 00). Distances are between effective field boundaries. The positioning of beam position monitors (MON) and steering magnets (SM) could be modified slightly (i.e. a few cm either way) without serious effect.

Segment 1			Segment 2			Segment 3		
Begin	End	Len (m)	Begin	End	Len (m)	Begin	End	Len (m)
Target	Q1 in	1.06885	Seg. beg.	MD1 out	0.4663	Seg. beg.	ED1 out	0.3527
Q1 in	Q1 out	0.2523	MD1 out	Ch. slit	0.3079	ED1 out	Mass slit	1.05
Q1 out	Q2 in	0.256925	Ch. slit	SM1 in	0.272			
Q2 in	Q2 out	0.33385	SM1 in	SM1 out	0.256			
Q2 out	MD1 in	0.638075	SM1 out	S1 in	0.1862			
MD1 in	Seg. end	0.4663	S1 in	S1 out	0.1875			
			S1 out	Q3 in	0.1614			
			Q3 in	Q3 out	0.3338			
			Q3 out	Q4 in	0.2162			
			Q4 in	Q4 out	0.3338			
			Q4 out	Q5 in	0.2162			
			Q5 in	Q5 out	0.3338			
			Q5 out	S2 in	0.1614			
			S2 in	S2 out	0.1875			
			S2 out	MON1	0.3092			
			MON1	ED1 in	0.50			
			ED1 in	Seg. end	0.3527			
Total		3.0163	Total		4.7819	(next table)		

2.1.1 Extracting optical parameters from field maps

This document describes how we have extracted the parameters necessary for the ion optical codes GIOSP and RAYTRACE from the field maps of quads and magnetic dipoles made of Doug Evans. A quadrupole is characterized by having a field whose magnitude varies linearly with the distance along a radius from its centre. Ion optical codes require 4 pieces of information to describe a quadrupole;

1. Poletips represent equipotential boundaries (below saturation) and the field magnitude there determines the strength of the setting

2. the bore or distance between opposite poletips

3. the effective length

4. the form of the fringing field, supplied as Enge coefficients for RAYTRACE and as fringing field integrals for GIOSP.

Using the field maps made by Doug Evans we make best estimates for effective lengths and fringing fields. Effective lengths are calculated from the same data used

Table 2.4: E.M.S. element spacings in the second stage (file reso2000.dat 28 Sept 00). Distances are between effective field boundaries.The positioning of beam position monitors (MON) and steering magnets (SM) could be modified slightly (i.e. a few cm either way) without serious effect. The quoted effective lengths of the steering magnets are not critical and could be reduced.

Segment 3			Segment 4			Segment 5		
Begin	End	Len (m)	Begin	End	Len (m)	Begin	End	Len (m)
Mass slit	SM2 in	0.277	Seg. beg.	MD2 out	0.6238	Seg. beg.	ED2 out	0.7883
SM2 in	SM2 out	0.256	MD2 out	MON3	0.56076	ED2 out	MON5 in	0.425
SM2 out	Q6 in	0.27085	MON3	SM3 in	0.1205	MON5 out	SM4 in	0.3155
Q6 in	Q6 out	0.2523	SM3 in	SM3 out	0.259	SM4 in	SM4 out	0.259
Q6 out	Q7 in	0.25695	SM3 out	Q8 in	0.24084	SM4 out	Q9 in	0.12
Q7 in	Q7 out	0.3338	Q8 in	Q8 out	0.3338	Q9 in	Q9 out	0.467
Q7 out	S3 in	0.1581	Q8 out	S4 in	0.1581	Q9 out	Q10 in	0.199
S3 in	S3 out	0.199	S4 in	S4 out	0.199	Q10 in	Q10 out	0.467
S3 out	MON2	0.098	S4 out	MON4	0.15	Q10 out	Final	1.176693
MON2	MD2 in	0.353	MON4	ED2 in	0.701			
MD2 in	Seg. end	0.6238	ED2 in	Seg. end	0.7883			
Total		4.4815	Total		4.1351	Total		4.2975

to calculate the fringing fields. Using a cubic spline interpolation of the data, B_{interp}, the effective length is calculated as,

$$L_{eff} = \int_{z_{min}}^{z_{max}} \frac{B_{interp}}{B_{max}} dz, \tag{2.1}$$

where the fields are vanishingly small at z_{min} and z_{max}. Since these ion optical codes both base their calculations on the axial field gradient, we would like to estimate them as close as possible to the axis. However, since the field disappears there, it is necessary to estimate the axial gradient from measurements of the field strength made at some finite distance from it. Also, since the survey axis does not necessarily coincide with the true magnetic axis, data from longitudinal scans made at equal distances from the survey axis are combined as,

$$B_{data} = \frac{B(x) - B(-x)}{2}, \tag{2.2}$$

where x is has been chosen as small as available. The longitudinal survey of the "Smit-Elma" quad, Q9, includes measurements of the field in the horizontal plane at .25 inch intervals. We have chosen x to be 1 inch in this case as a tradeoff between signal to noise and distance from the axis (6.25 inch bore). The Q2 survey includes a scan at x=1.5 inch. All other surveys have longitudinal scans at distances from the axis that correspond to the radii of the rotating coil surveys. Fringing fields are obtained by fitting the following Enge function, E(s), to the data,

$$\frac{B(s)}{B_{max}} = \frac{1}{1+\exp\left(-E(s)\right)}, \tag{2.3}$$

$$E(s) = \sum_{i=0}^{5} e_i s^i, \tag{2.4}$$

where the dimensionless s=z/L and L is either a dipole gap or the bore of a quadrupole. The best fit is obtained by holding e_0 constant and allowing the other 5 coefficients to vary. The optimization can be made in one of two ways; either by fixing e_0 equal to a value obtained from the above estimation of L_{eff},

$$e_0 = \ln\left(\frac{B_{max}}{B_{interp}\left(\frac{L_{eff}}{2}\right)} - 1\right), \tag{2.5}$$

and then varying e_0 manually until the following integral identity, that places the effective field boundary at the origin for this combination of parameters (i.e. s_{min},s_{max} and e_0),

$$\int_{s_{min}}^{s_{max}} \frac{B(s)}{B_{max}} ds = -s_{min}. \tag{2.6}$$

2.1.2 First order optics

Superficially, the DRAGON separator consists of 2 stages of mass separation, each utilizing a magnetic followed by an electric bender or symbolically; MD_1,ED_1/MD_2,ED_2. Key locations of the optics design are: the charge-selection slits following dipole MD1, the mass-selection slits following ED1, and the final slits. Horizontal images exist following each of the 4 benders.

The DRAGON separator has 3 horizontal and 2 vertical intermediate images between the gas target centre, labelled T, and the final focal plane, labelled F. Pairs of X and Y slits are located at the first 2 horizontal intermediate image points, the charge slits, labelled Q, and the mass slits, labelled M and the final focus F. Table 2.6 lists first-order transfer matrix elements between the target centre and each of these three slit locations and at the horizontal image following MD2.

Table 2.5: Field strengths for rigidities 0.5 T·m and 8 MV scaled from the GIOS input file reso2000.dat Tunes must be obtained by scaling to the rigidities of a given reaction.Note that the sextupole strengths have been scaled to the new L_{eff} values listed in table 1.2.

Element	Gap or Diam.	Effective length	Field
Q1	10.8 cm	25.23 cm	-2.187 kG
Q2	15.9 cm	33.385 cm	+2.003 kG
S0	15.9 cm	33.385 cm	+0.106 kG
MD1	10 cm		+4.991 kG
S1	15.9 cm	18.75 cm	+0.425 kG
Q3	15.9 cm	33.38 cm	+1.826 kG
Q4	15.9 cm	33.38 cm	-2.412 kG
Q5	15.9 cm	33.38 cm	+1.329 kG
S2	15.9 cm	18.75 cm	+0.089 kG
ED1	10 cm		±200. kV
Q6	10.8 cm	25.23 cm	-1.181 kG
Q7	15.9 cm	33.38 cm	+1.696 kG
S3	16 cm	19.9 cm	+0.047 kG
MD2	12 cm		6.139 kG
Q8	15.9 cm	33.38 cm	+1.257 kG
S4	16 cm	19.9 cm	+0.360 kG
ED2	10 cm		±160. kV
Q9	15 cm	46.7 cm	-0.972 kG
Q10	15 cm	46.7 cm	+1.087 kG

Table 2.6: GIOS First-order transfer matrix elements at the four horizontal image points (file reso2000.dat 28 Sept 00): x is horizontal position (m); a is horizontal angle (rad); y is vertical position (m); b is vertical angle (rad); d is fractional energy difference; g is fractional mass difference; t is fractional difference in time-of-flight.

	Charge	Mass	Charge′	Final
(x|x)	-0.440	0.689	-0.580	0.980
(x|a)	0.000	0.000	0.000	0.000
(x|g)	0.302	-0.472	-0.472	-1.828
(x|d)	0.302	0.000	0.684	0.000
(a|x)	-1.648	1.147	-2.122	0.052
(a|a)	-2.273	1.451	-1.725	1.020
(a|g)	0.401	-0.321	1.589	1.303
(a|d)	0.401	0.015	0.669	-0.022
(t|x)	0.172	0.002	0.161	-0.002
(t|a)	0.368	0.000	0.179	0.000
(t|g)	0.515	0.504	0.462	0.515
(t|d)	-0.485	-0.492	-0.482	-0.477
(y|y)	-3.554	0.980	3.487	-1.767
(y|b)	0.018	-0.430	0.227	0.000
(b|y)	-1.563	2.307	-3.336	1.657
(b|b)	-0.273	0.008	0.070	-0.566

As may be seen from the values of the matrix elements, there exist simultaneous horizontal and vertical images at the Q and F slits locations only(i.e. (x|a)=0 and (y|b)=0 at these locations). The vertical condition at the M slits has been chosen to limit the vertical extent of recoils at the M slits, thereby reducing possible transmission of scattered beam, while at the same time minimizing the extent of the height of the recoils throughout the separator in order to minimize and allow the reduction of residual horizontal aberrations using sextupoles (without introducing unacceptable vertical aberrations as a result).

Optically it makes sense to group the optical elements that transfer one horizontal image point to the next. Accordingly, we can consider the first stage of DRAGON as broken into 2 substages; from the gas target centre T, through (Q_1,Q_2 + MD_1) to the Q-slits and from there through (Q_3,Q_4,Q_5 + ED_1) to the M slits.

When tuned on the charge state Q_t there is a momentum/charge dispersed focus at the Q slits and an achromatic focus at the M slits which shows dispersion in mass/charge. Defining from the target to the Q slits an energy/charge dispersion D_1=(x|d) and linear magnification M_1=(x|x) and similarly from Q to M slits, D_2=(x|d) and M_2=(x|x). In the first substage, the mass/charge dispersion, (x|g) = (x|d), while in the second (x|g) = 0. The relationship between the above quantities can be clarified

by considering the following matrix representation of the map transferring particles in the horizontal plane, from the target (T) to the mass slits (M), expressed as the product of the maps of the two substages,

$$\begin{bmatrix} x \\ a \\ d \\ g \end{bmatrix}_M = \begin{bmatrix} M_2 & 0 & D_2 & 0 \\ - & 1/M_2 & - & - \\ 0 & - & 1 & 0 \\ 0 & - & 0 & 1 \end{bmatrix} \begin{bmatrix} M_1 & 0 & D_1 & D_1 \\ - & 1/M_1 & - & - \\ 0 & - & 1 & 0 \\ 0 & - & 0 & 1 \end{bmatrix} \begin{bmatrix} x \\ a \\ d \\ g \end{bmatrix}_T . \tag{2.7}$$

For clarity, elements that don't concern the present argument are left as "-". So the overall mass/charge dispersion for the first stage (T to M) is D_1*M_2 + 0. The overall magnification is M_1M_2, and so the first-stage (first-order) mass resolving power(MRP) is (for unit size of target object),

$$\frac{m}{\Delta m} = D_1 \left(\frac{M_2}{M_1 M_2} \right) = \frac{D_1}{M_1}. \tag{2.8}$$

So the MRP of the first stage can be thought of as set entirely by the quads and dipole lying between the target and Q slits (including the distance to the Q slits after the dipole). The achromatic condition at the M slits imposes D_2/M_2 = -D_1. One can think of the field strengths of Q_1,Q_2 giving the desired Q-slit focus and first-stage MRP and the triplet Q_3,Q_4,Q_5 then producing the achromatic focus plus one other condition at the M slits.

The second stage can be thought of in much the same way, the horizontal image location following MD_2, referred to as $Q^{'}$, being analogous to Q in the first stage. As may be seen in Table 2.6, the first order mass resolving power of the second stage is larger than that of the first stage.

2.1.3 Second and higher order optics

In order to improve the mass resolving power of each stage the images at the M and F slits locations have been partially corrected to second order. As stated above the vertical extent has been limited as much as possible to reduce the contribution of aberrations from the dipole entrance and exit fringing fields and provide locations where horizontal aberrations may be reduced without unduly increasing vertical aberrations. This is done in the first stage by shaping the pole pieces of Q_2 (to contain a sextupolar pole tip field 5.5% that of the quadrupolar value) and the discrete sextupoles S_1 and S_2. The sextupole in Q_2 is ideally placed to reduce the spherical aberration (x|aa) at the M slits. An octupole moment included in Q2, while effective in reducing the (x|aaa) aberration at the M slits, would not result in an appreciable narrowing of the image there. These 3 sextupolar strengths also combine to reduce the chromatic aberrations (x|ad) and (x|dd) there. In the second stage S_3 and S_4 combine to reduce the aberrations (x|aa) and (x|ad) at the F slits. Unfortunately, no location was found that allowed for the simultaneous reduction of (x|dd). This appears to be an unavoidable

Table 2.7: GIOS Some second-order transfer matrix elements at the four horizontal image points (file reso2000.dat 28 Sept 00): x is horizontal position (m); a is horizontal angle (rad); y is vertical position (m); b is vertical angle (rad); d is fractional energy difference; g is fractional mass difference; t is fractional difference in time-of-flight.

	Charge	Mass	Charge′	Final
(x|xx)	-7.128	-3.805	-7.687	-6.110
(x|xa)	-20.063	-4.003	-15.961	-1.175
(x|xg)	1.851	2.778	10.462	1.410
(x|xd)	1.851	1.994	2.190	0.773
(x|aa)	-14.488	0.180	-8.700	4.007
(x|ag)	3.008	1.283	10.051	4.045
(x|ad)	0.302	-0.425	4.004	-0.713
(x|gg)	-0.213	-0.208	-3.648	-8.632
(x|gd)	-0.123	-0.900	-1.026	-10.510
(x|dd)	-0.213	-0.661	0.082	-3.548
(x|yy)	-5.004	109.0	-0.933	15.152
(x|yb)	-0.247	11.82	-12.221	22.422
(x|bb)	0.493	-0.412	0.314	-0.029

consequence of the first order design of the second stage. Table 2.7 lists second-order transfer matrix elements between the target centre and each of these three slit locations and at the horizontal image following MD2.

The effective mass resolving powers of the first and second stages with the DRAGON separator tuned on a given recoil product are necessarily smaller than the first order values due to the presence of aberrations and the constraint of assuring a sufficiently high overall recoil transmission to the end detectors. Reaction independent first order MRP and the effective ^{19}Ne mass resolving powers are compared in Table 2.8. In both cases the values for the MRP are given by the mass dispersion of each stage divided by the image size at the M and F focal planes. A full width of 5 mm at the gas target centre was assumed. Note that the first order image size for the second stage is the original image size multiplied by the second stage magnification, $(x|x)_2=(x|x)_F/(x|x)_M$. For the effective MRP values the image sizes were taken to be equal to full slit widths, given in Table 3.1, that were used in the simulations of ^{19}Ne recoils described below.

2.1.4 Aberrations

The increase in beam-spot size at the Mass slits due to aberrations will be different for different reactions, because the size of an aberration term depends upon products of initial position, angle, and energy deviations from the central values. A reaction such

Table 2.8: First order and effective mass resolving powers for ^{19}Ne recoils.

MRP	stage 1	stage 2
1st order	137	190
effective	91	150

as ^{15}O(α, γ)^{19}Ne has larger recoil cone angle, kinematic energy spread, and beam spot size than, say, ^{25}Al(p, γ)^{26}Si and so has larger optical aberrations.

The design criterion defining an "acceptable" level of aberrations is that the half-width of aberration terms at the Mass or Final slits should be less than 10% of the mass separation of beam and recoil product at the Mass slits and 5% of their separation at the Final slits. An additional condition at the Final slits is that the aberration terms should be no larger than the combined contribution of first-order terms. These criteria are arbitrary, in that it cannot be demonstrated that they are necessary and sufficient to achieve 10^{10} suppression of background.

The geometric and chromatic aberrations computed by GIOS are "unavoidable" consequences of the ion-optical properties of dipoles and quadrupoles. To correct them requires addition of sextupole (or higher multipole) elements or modification of field boundaries to induce multipole terms. In addition, there will be "avoidable" contributions due to mechanical imperfections of the elements, to their misalignment, to deviations between ideal design fields and real field profiles, to incorrect field settings, or to instability in power supplies.

The allowable limits on "avoidable" aberrations have been determined by RAYTRACE simulations, as follows:

- misalignment (rotation, displacement) of elements
- incorrect field strengths
- mechanical imperfections (parallelism of dipole faces, concentricity and freedom from twist in quadrupoles)
- non-ideal field profiles

Chapter 3

RAYTRACE simulation results

The optics of the DRAGON has been studied for ^{19}Ne recoils which have the largest expected spread in momenta of the radiative capture reactions of interest. The DRAGON recoil separator has been designed in order to allow the $^{15}O(\alpha,\gamma)^{19}Ne$ reaction rate to be determined to an overall accuracy of 20%. This design goal has been tested by simulating, as accurately as possible, the initial positions and momenta of ^{19}Ne recoils. A GEANT simulation of a He gas target of 1.5 Torr was made, which includes the effects of a beam with the expected transverse and longitudinal emittances focused to a finite sized waist at the gas target centre and multiple scattering (i.e. Moliere angular distributions, energy loss and straggling throughout the paths of the ^{15}O ion and the recoiling ^{19}Ne ion), as well as the width of the resonance and the branching ratios of the gammas emitted by the compound nucleus, $^{19}Ne^*$. The coordinates that are used as input to RAYTRACE are those of particles that left the gas target without hitting any surfaces, back projected to the gas target centre (see MIG97 for more details). To estimate the geometrical acceptance another simulation was made of ^{19}Ne ions all having the central or tuned energy and starting from the gas target centre in directions that randomly filled a cone of half angle 25 mrad.

In the RAYTRACE input file, the gas target pumping tubes are represented by 2 circular apertures, the first of diameter 8 mm at the exit of the cell itself, 5 cm from its centre and a second aperture of 36 mm diameter at the end of the gas pumping tubes, 70 cm further downstream. This arrangement is meant to reproduce the effect of conical pumping tubes that extend from the 8 mm diameter gas target exit aperture at an opening angle of 20 mrad.

3.1 Phase space plots

Projections of the trajectories of ^{19}Ne ions from the full GEANT simulation onto x-z and y-z planes are shown in figure 3.6 for the latest tune of Sept. 2000, res2000.dat. The presence of the aberration $(x|\ \delta_E\delta_E)$, uncorrectable in the second stage, is evident in the plot shown in figure 3.5 of x position at the final slits versus initial energy, δ_E.

There are four horizontal image points in the DRAGON separator; one after each

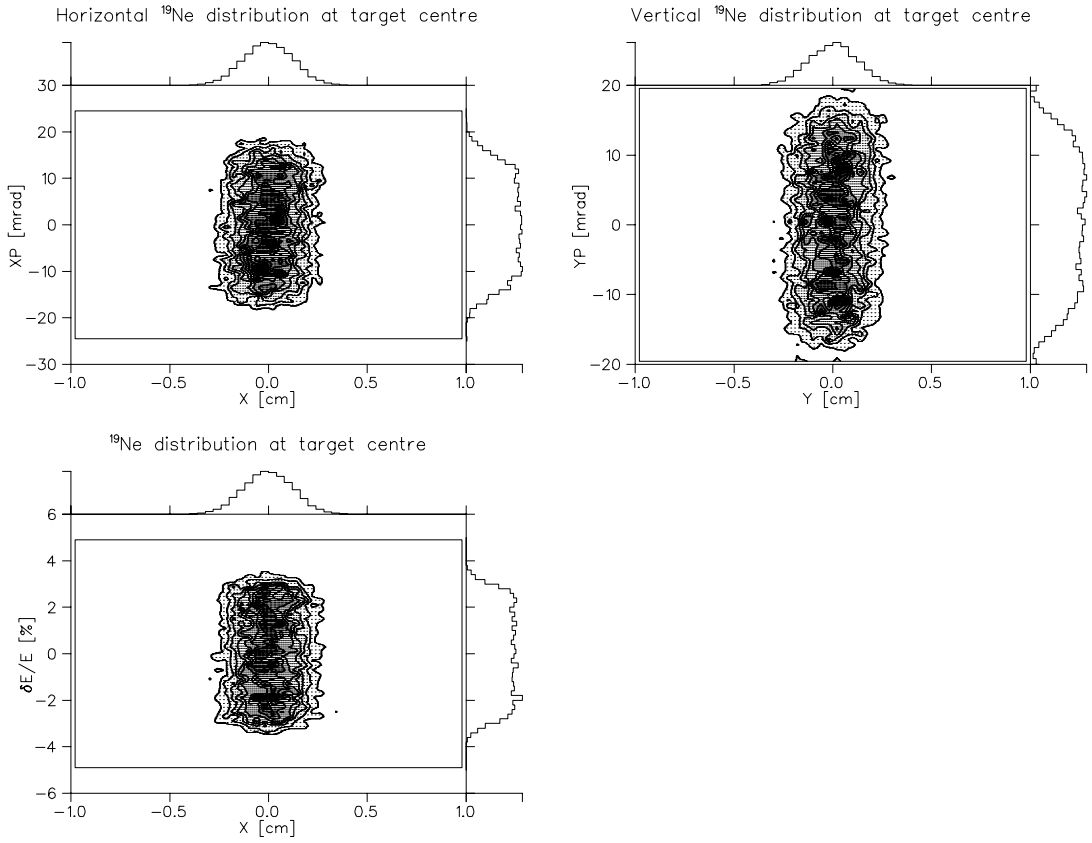

Figure 3.1: X and Y phase space plots and a plot of relative energy versus horizontal position at the gas target centre for 10000 simulated ^{19}Ne ion trajectories.

of the magnetic dipoles, and two others at the end of the first and second stages. In the following five figures plots of vertical and horizontal phase space as well as a plot of the relative energy versus the horizontal position are shown figures in 3.1,3.2, 3.3, 3.4 and 3.5 at the gas target each of the successive horizontal image points for^{19}Ne ions.

3.2 Acceptance

The acceptance of the DRAGON separator has been studied for both ^{19}Ne recoils and more traditionally, for a point source of ions of the tuned energy only, leaving the gas target centre in directions that uniformly fill a cone larger than its angular acceptance. The acceptance was studied for the apertures and slit settings shown in Table 3.1.

3.2.1 Geometrical acceptance

The geometrical DRAGON acceptance of ^{19}Ne ions having the central or tuned energy only is shown in figure 3.7 as a function of the polar lab angle of ions leaving the gas

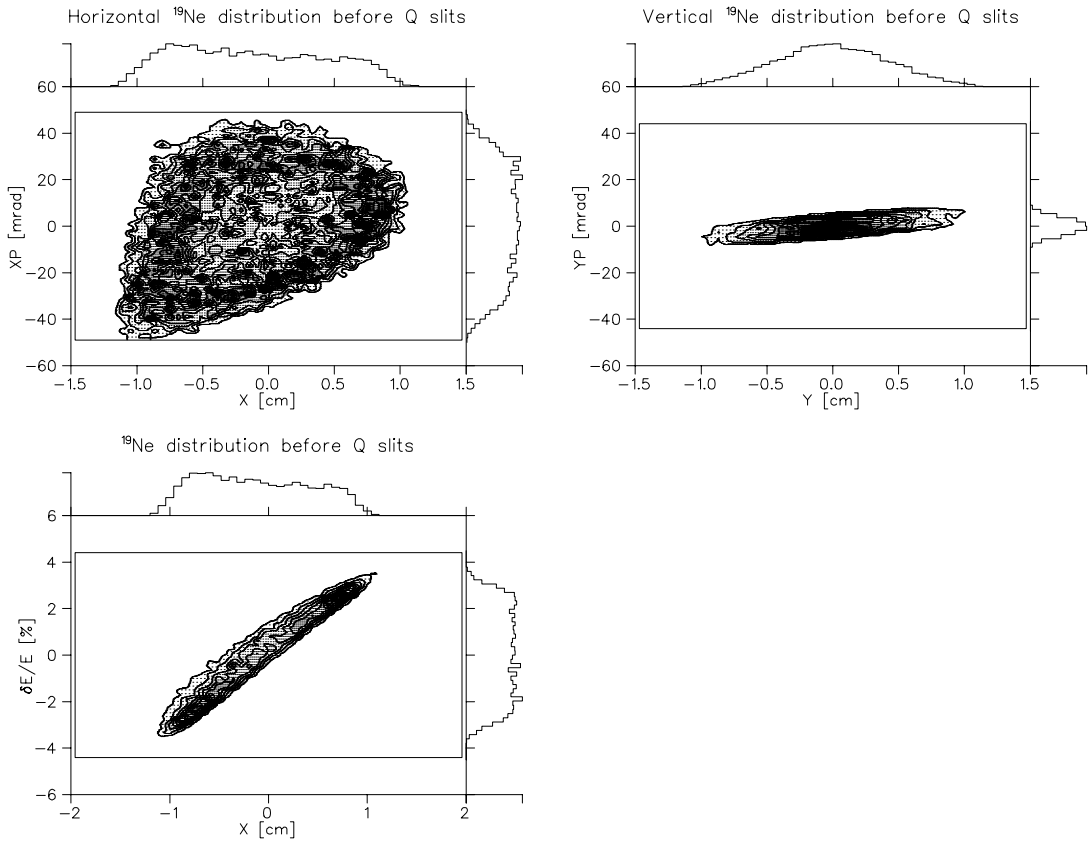

Figure 3.2: X and Y phase space plots and a plot of relative energy versus horizontal position at the charge slits for 10000 simulated ^{19}Ne ion trajectories.

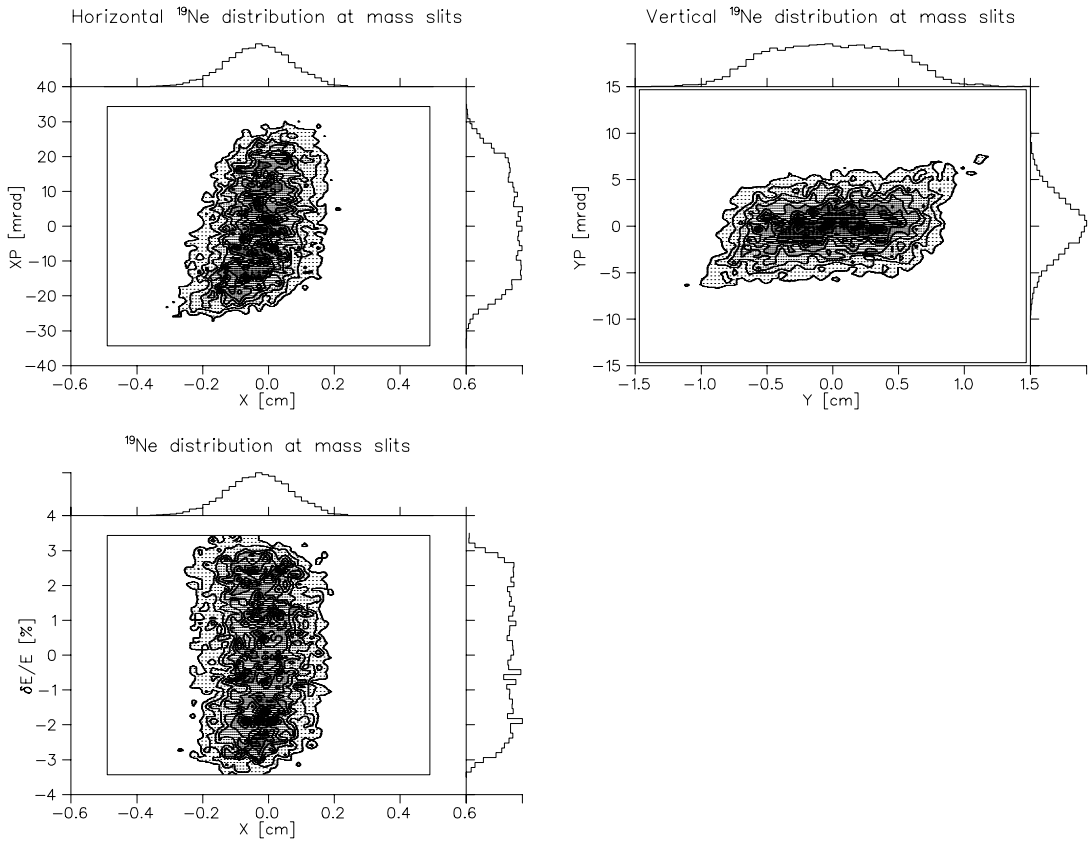

Figure 3.3: X and Y phase space plots and a plot of relative energy versus horizontal position at the mass slits for 10000 simulated ^{19}Ne ion trajectories.

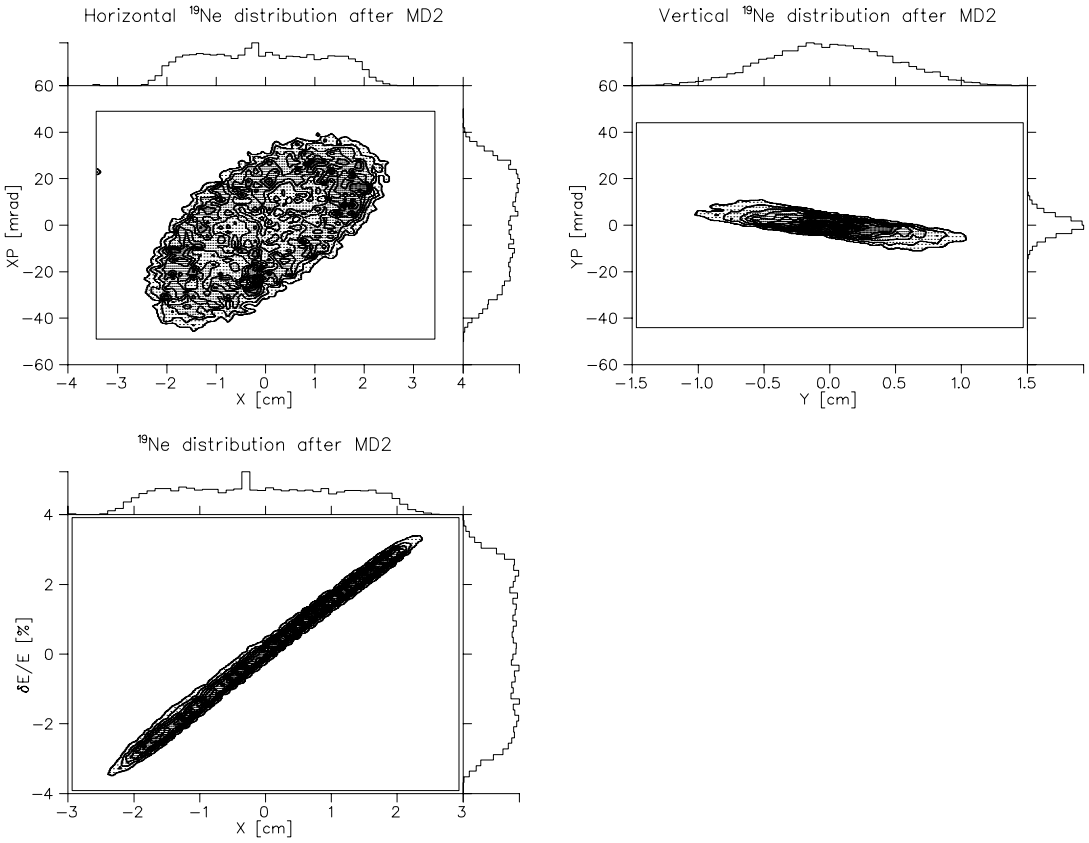

Figure 3.4: X and Y phase space plots and a plot of relative energy versus horizontal position at the horizontal image following MD2 for 10000 simulated ^{19}Ne ion trajectories.

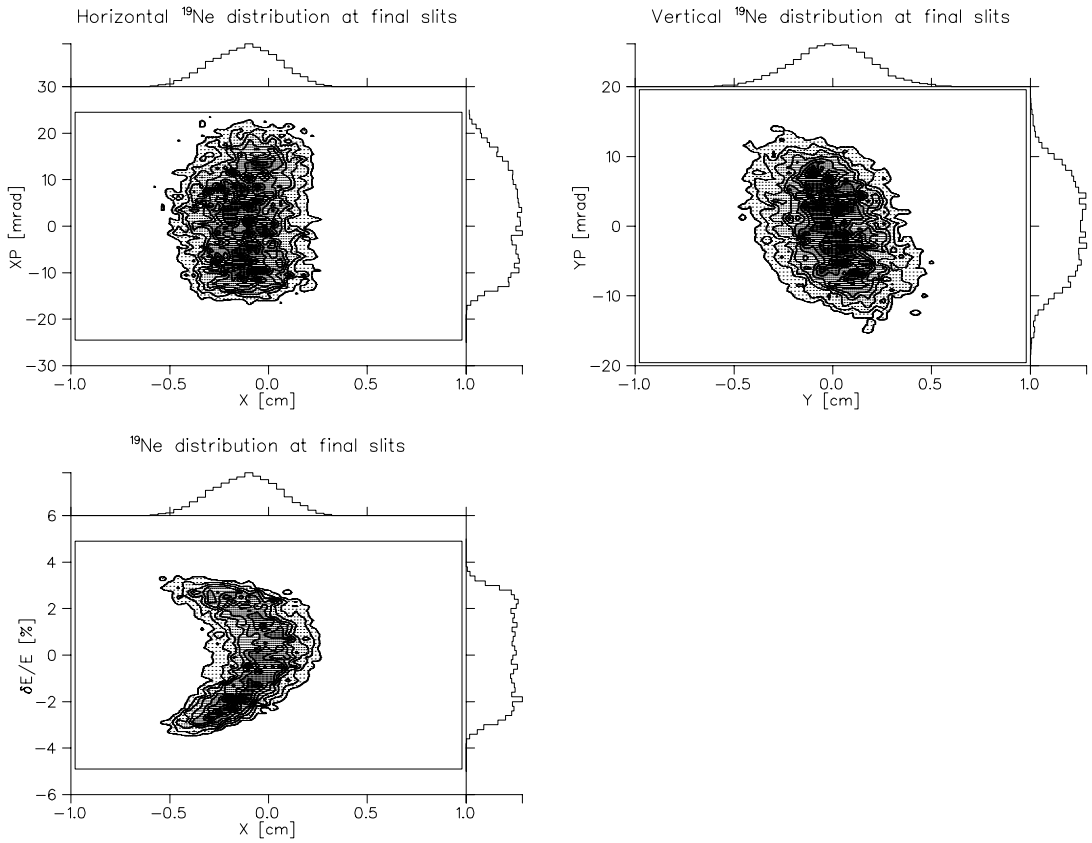

Figure 3.5: X and Y phase space plots and a plot of relative energy versus horizontal position at the final slits for 10000 simulated ^{19}Ne ion trajectories.

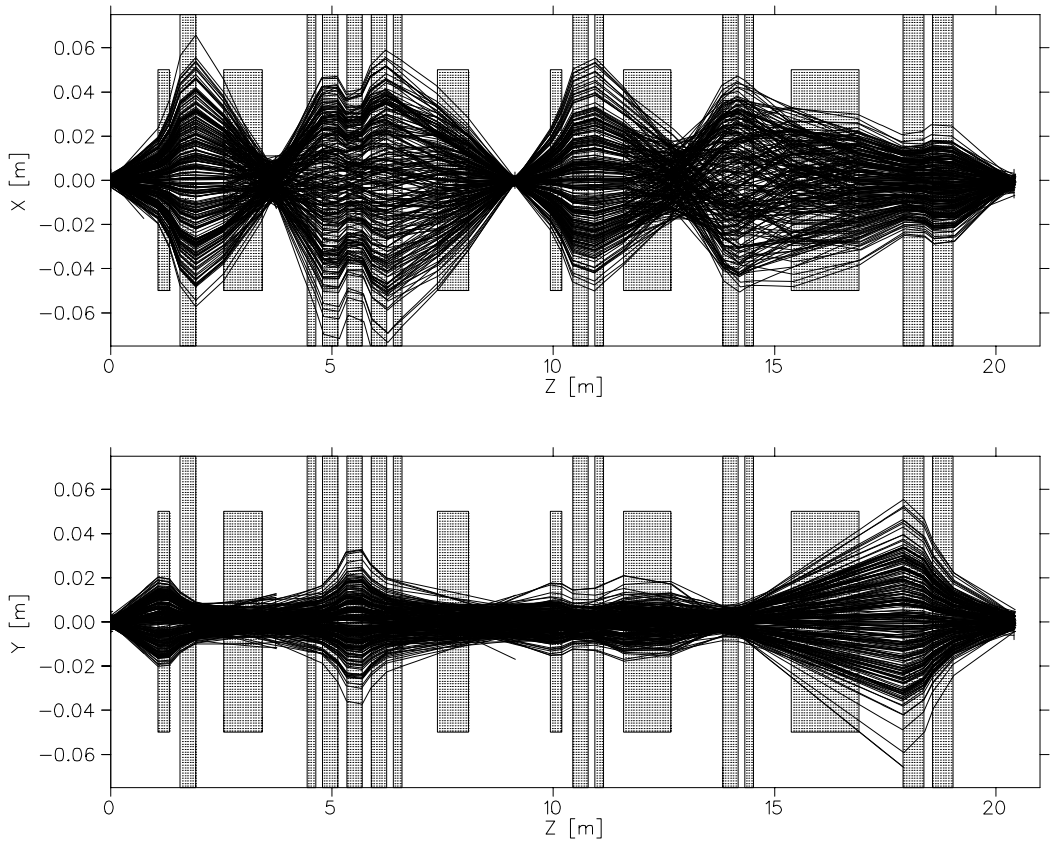

Figure 3.6: X and Y projections of 250 ^{19}Ne trajectories from the full GEANT simulation.

Table 3.1: Limiting apertures and slit widths used for ^{19}Ne acceptance calculations.

components	apertures(cm)
$Q_{1,6}$	10
$Q_{2..5}, Q_{7,8}$	15
$S_{1..4}$	15
$Q_{9,10}$	15
$Q_{9,10}$	15
MD_1	8(y)
MD_2	9(y)
ED_1	10(x)
ED_2	10(x)
gas target collimators	diameter in cm
entrance	0.8
exit	3.6
slit location	full width x(y) in cm
Q	2.32(2.2)
M	0.48(2.4)
F	0.92(1.2)

target centre from a point source. Initial polar lab angles are distributed uniformly over a cone of half angle 25 mrad. The curve represents the probability of an ion passing through the final slits. The cutoff at 24 mrad corresponds to the angle subtended by a line drawn from the gas target centre to the exit aperture of the gas target pumping tubes and the optical axis.

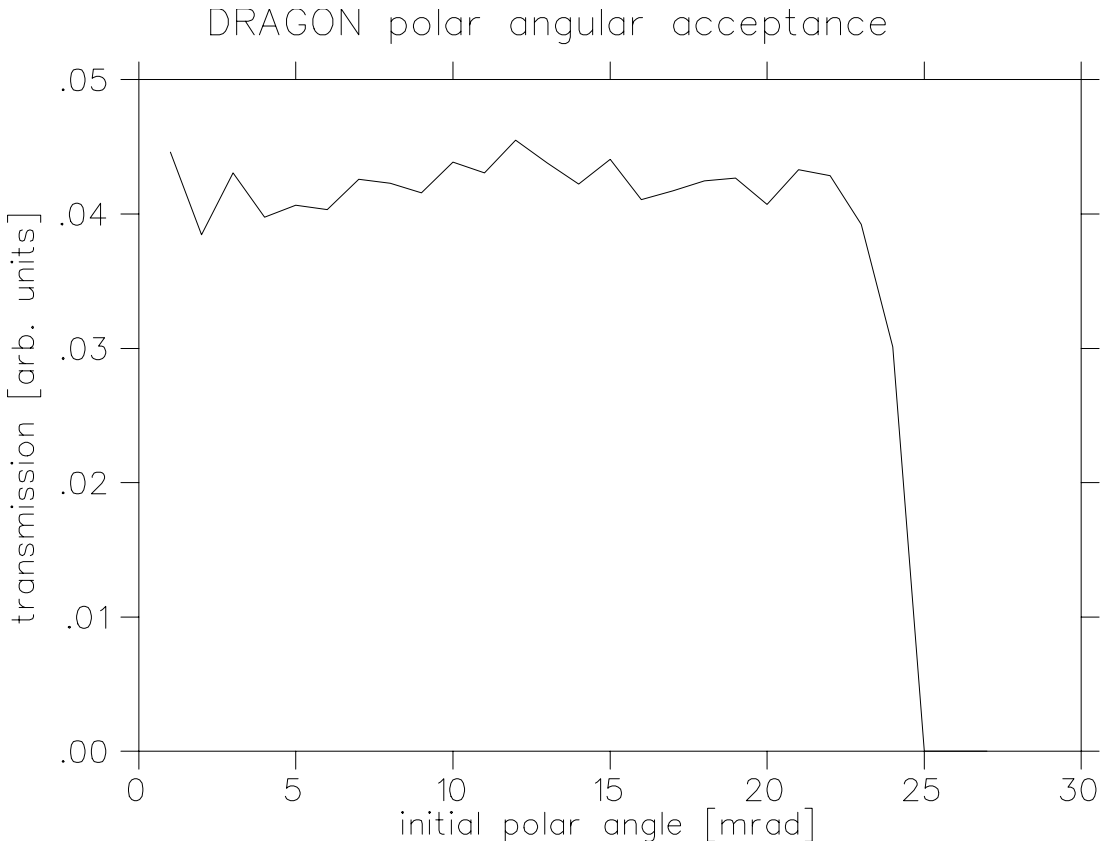

Figure 3.7: ^{19}Ne acceptance of the DRAGON as a function of the initial polar lab angle. The curve represents the probability of transmission of ions of central energy only, whose initial polar lab angles are distributed uniformly over a cone of half angle 25 mrad.

The origin and form of the knee in figure 3.7 is better understood by considering the initial phase space of the ions that do not pass through the final slits, shown in figure 3.8. In this figure the distance from the origin represents the initial polar angle and the initial azimuthal angle is given by the angle between a line joining a point to the origin and the positive abscissa (taken in the usual CCW sense). The circle represents the acceptance of the gas target pumping tubes. The points on the right hand size represent the initial directions of ions that did not enter ED_1 and the group on the left, those that hit the beam pipe passing through Q5. These ions were initially directed to the left and right respectively, as viewed from the gas target centre along the optical axis.

3.2.2 ^{19}Ne recoil acceptance

The acceptance of ^{19}Ne recoils is reduced compared to the above due to;

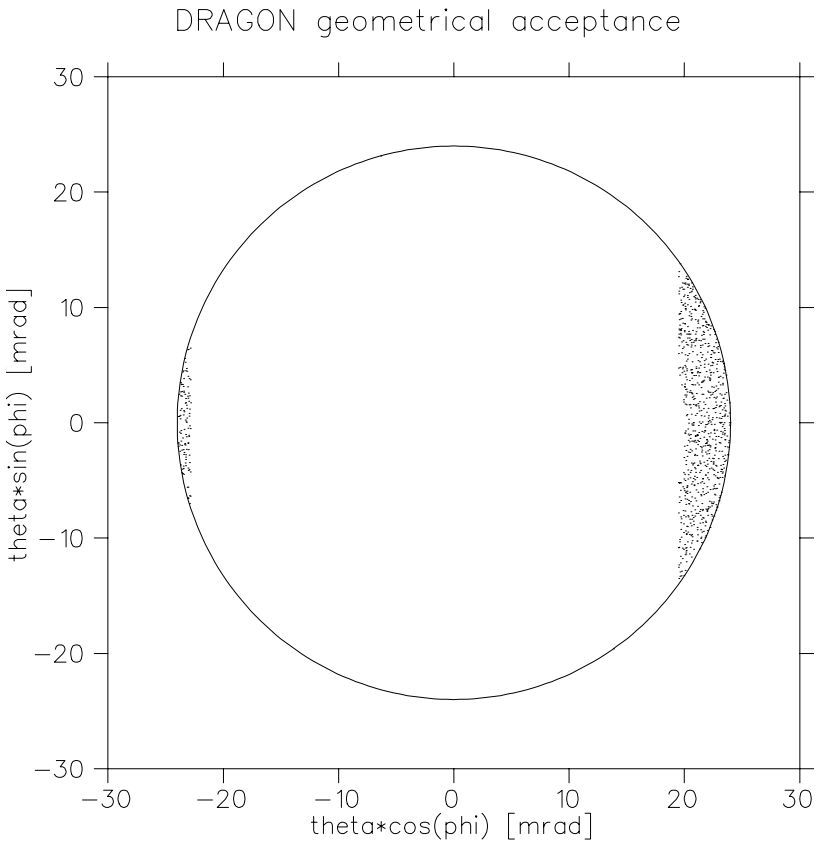

Figure 3.8: Polar representation of the geometrical acceptance of the DRAGON.The points represent the initial polar (distance from radius) and azimuthal (usual convention) angles of ions that do not pass through the final slits. The circle represents the acceptance of the gas target collimators.

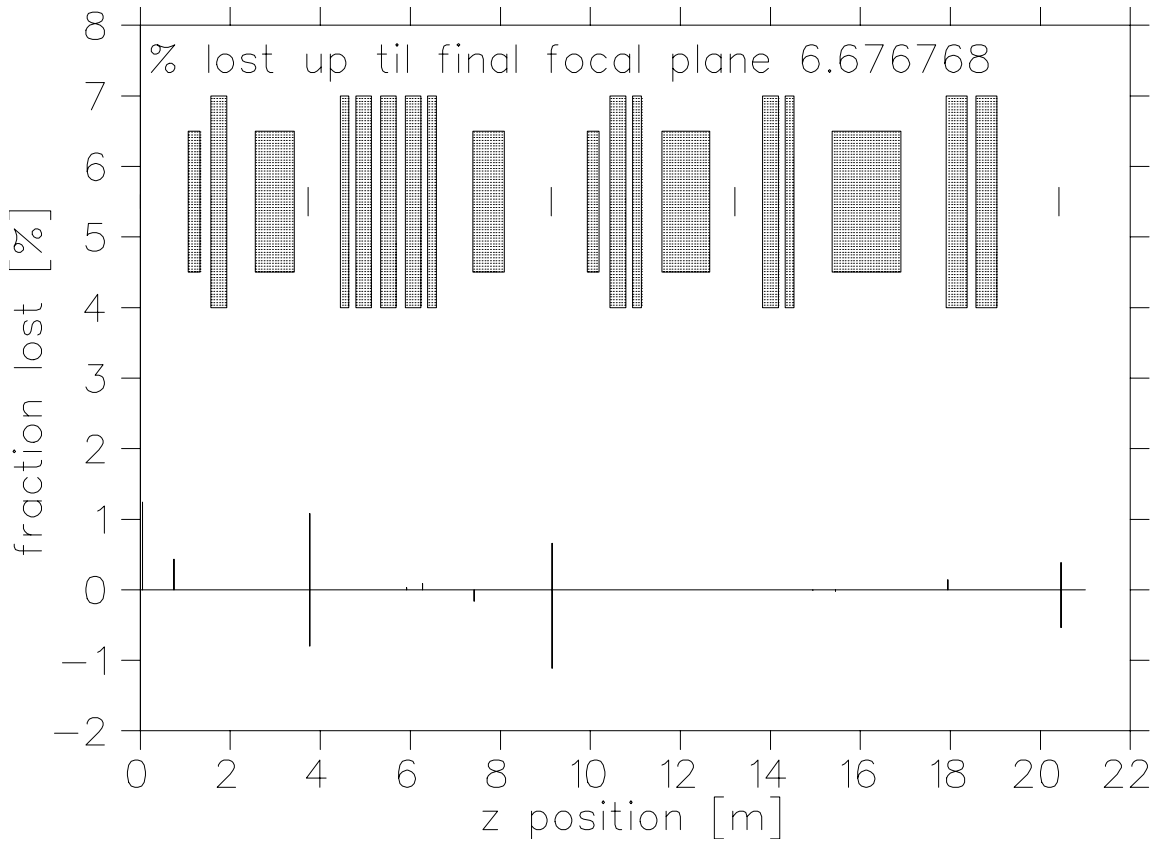

Figure 3.9: Percent ^{19}Ne losses along the DRAGON. For the slits and dipoles, vertical and horizontal losses are indicated by positive and negative values respectively.

- the finite source size at the gas target centre and
- the energy spread and its correlation with polar angle.

A plot showing the percent loss of ^{19}Ne ions (GEANT simulation) along the optical axis is shown in figure 3.9. As may be seen the slit settings have been chosen so that losses are limited to no more than about 2 % loss for each pair of X and Y slits located at the charge, mass and final focal planes.

In figure 3.10 the solid curve represents the relative fraction of ^{19}Ne ions leaving the gas target that pass through the final slits as a function of the initial polar angle. The dashed curve shows the relative fraction of ^{19}Ne ions leaving the gas target that are NOT transmitted through the final slits.

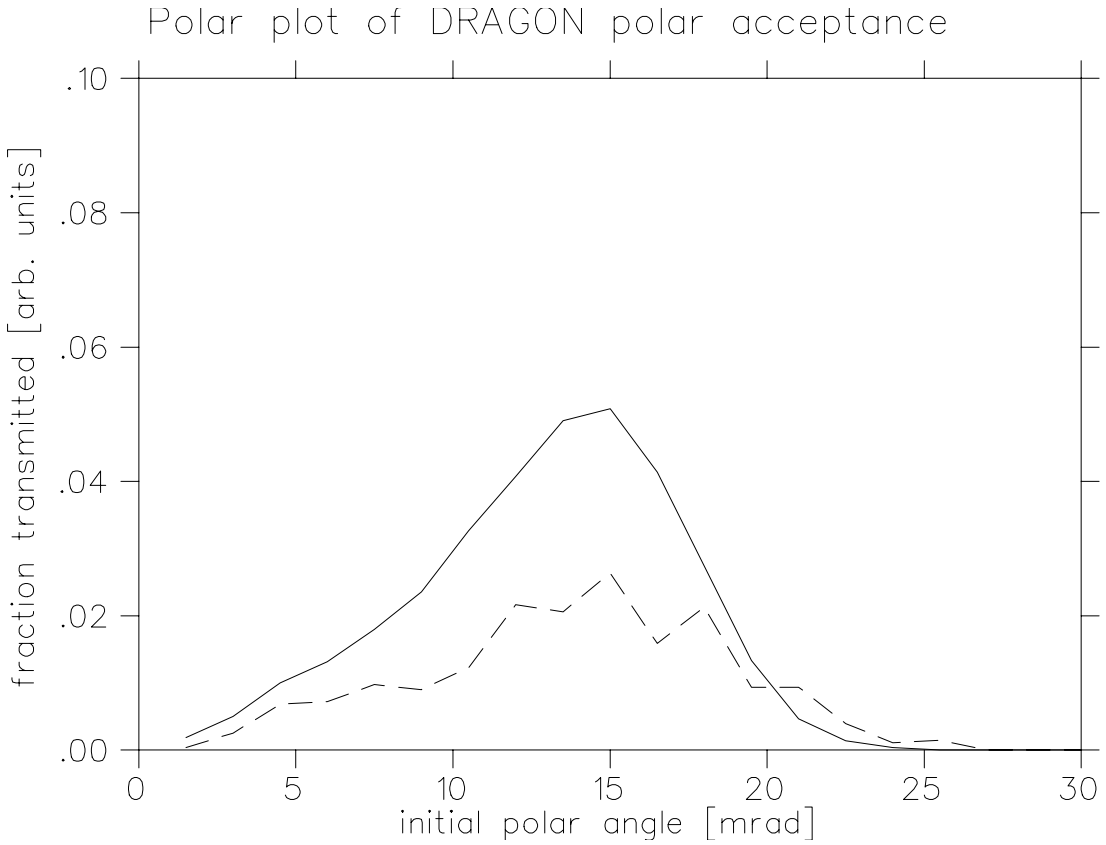

Figure 3.10: The solid curve represents the relative fraction of ^{19}Ne ions leaving the gas target that pass through the final slits as a function of the polar angle. The dashed curve shows the relative fraction of ^{19}Ne ions leaving the gas target that are NOT transmitted through the final slits. Note that the vertical scale for the dashed curve has been expanded by a factor of 10 for clarity.

Chapter 4

Background suppression

The chief source of background is expected to be beam particles which have charge-changing and/or scattering collisions inside the E.M.S.(ElectroMagnetic Separator), such that they are transmitted to the recoil ion detector at the end of the E.M.S. Some processes such as Coulomb scattering or charge-changing collisions with residual gas may be modeled with factor-of-two uncertainties in cross section. Scattering from solid surfaces is much harder to estimate. Simulations show that no single deflection, charge-change or energy loss occurring before the Charge Slits should allow beam particles to pass cleanly through the Final Slits. Sequences of two scatterings at just the 'right' locations may pass beam particles through the Final Slits, however. There is no reliable way to demonstrate *a priori* that the E.M.S. design meets the design specification of beam suppression by 10^{10}.

(An isobaric contaminant in the beam (e.g. ^{15}N in beam of ^{15}O) may give rise to a capture reaction, the recoil product of which is less than a part per thousand different in mass from the desired recoil product. The E.M.S. provides no useful mass separation at the part-per-thousands level.)

Suppression of background will be aided by

- optics design which provides good mass resolving power at the Mass slits and the Final slits, and by keeping aberrations small in comparison to first-order contributions due to beam emittance

- keeping slits as thin as is consistent with ion stopping ranges (less than 10 μm) and with mechanical strength

- coating slits with low-Z material

- installing traps or baffles to prevent beam particles from hitting vacuum surfaces at oblique angles (this will not be possible on high-voltage electrodes)

- maintaining low residual-gas pressures, especially in regions which have been identified as 'sensitive' by simulation programs (electrostatic dipoles)

Simulations of elastic scattering made using RAYTRACE of charge-changing collisions (CCC for short) and truncated Rutherford scattering, were both forced to take place when an ion reaches a given value of the longitudinal coordinate z.

Inelastic scattering of beam was simulated by making Monte Carlo "shotgun" simulations of beam starting from either the Q or M slits with uniformly distributed initial angles and energy between full and half beam energy. Of particular interest is the section between charge and mass slits, where nearly half the beam intensity remains.

4.1 Charge-changing collisions

Charge-changing collisions of beam ions on residual gas molecules have cross sections which typically are 10–100 times greater than for problem-causing Rutherford scatterings. However, a jump in charge results in a corresponding change in rigidity and an ion passing through a dipole with another charge will usually be swept aside.An excellent review of charge changing phenomena has been made by Betz [2]. Data and estimates exist for total cross sections. The momentum of the incident ion was assumed to be unaffected by its encounter with the residual gas molecule. The possibility that beam particles can suffer sequential charge changing collisions that results in their passing through the final slits of the DRAGON has been investigated substage by substage. We began by considering the high mass case ^{25}Al(p,γ)^{26}Si, tuned on q=8 ^{26}Si, for which the separation of beam in product is relatively small at the mass slits. A single electron pickup event from q=9 to 8 taking place in the region just after Q1 to near the end of Q2 was found that results in partial transmission of events through the mass slits. The probability of transmission through the mass slits in this case, despite the relatively greater pressure expected so close to the gas target, is relatively small compared to the following case however. Investigating the same tune it was found that near total transmission of beam through the mass slits occurs when single electron loss (due to a CCC or decay in flight), from the tuned value, q to q+1, takes place in the appropriate region of the electrostatic(ED) dipole ED1. Similarly, electron loss in ED2 would allow transmission of any full energy beam that reaches ED2 on trajectories close to the optical axis. This weakness of ED dipoles is due to the fact that (for all but the tunes on q=4 or higher in the ^{15}O(α,γ)^{19}Ne case for which q and q+2 are the culprits) the electric rigidities of these beam charge states are higher and lower than that of the product. For a magnetic dipole, the pair of beam charge states that straddle the product rigidity in this way are q-1 and q+1. The approximate location in the dipole ED1, x, expressed as a fraction of its length L, for which an on axis beam particle of mass A and of the tuned charge state q losing n electrons results in zero deflection of beam of charge state q+n leaving ED1 is,

$$x_{loss} = \frac{L}{1 + \frac{\frac{A_{cap}}{A}}{1 - \left(1 + \frac{A_{cap}}{A}\right)\frac{q}{q+n}}},$$

where A_{cap} is the mass of the captured particle. As an example,a q = 4 to 6 change for ^{15}O occuring at a distance 490/19 = 25.8 cm from the entrance of ED1 would be transmitted through the mass slits. Calculations locate the maximum transmission near 26 cm with a FWHM of about 3.5 cm. In all cases, such full beam energy ions are deflected by MD2 due to their reduced rigidity. Transmission through the final slits by CCC alone would require 3 successive events; electron loss in ED1 followed by a pickup event before or slightly into MD2 and finally electron loss in ED2. We have considered up until now, only low impact parameter charge changing events for which there is negligible momentum transfer, i.e. events leaving trajectories and energies unchanged. One would expect that events involving closer encounters would result in an angular broadening and shifting to lower energies of q=4 ^{15}O ions reaching the final focal plane. While lower energy ions would fall further from the slits, exactly what this would do to the distribution of ions at the final focal plane is difficult to predict.

4.1.1 CCC cross section estimates

No data for the equilibrium charge distributions of ^{15}O and ^{19}Ne ions on a He gas target are available in our energy range (at least in the collection of data [6]). Some idea of the average charge states that may be obtained from the C foil data of [5], which gives close to 3.65 for both the 0.16 MeV/u beam and 0.1 MeV/u product. An inspection of gas target data from [6] with C foil data of [5] for other cases suggests that the equilibrium values for a He gas target would be no more than 1 charge state smaller. Very little differential cross section data for charge changing collisions exists.Cross sections were estimated from: for ^{15}O, [3] for electron loss and the collection of data of [4] for electron pickup(single and double) on a thin (i.e. only single events) He gas target. We use [4] to estimate cross sections in the case of ^{15}O on He residual gas. Due the strong energy dependence of the electron capture cross sections, reliable estimates from [3] can not be made. Values estimated from the empirical expression for electron capture of [7] are indicated with a superscript S in the table 4.1 below. This expression and for loss the expression due to [8] are used for ^{21}Na and ^{25}Al and compared with data for ^{15}O. Cross section estimates are summarized in Table 4.1,

The residual gas will presumably consist of the lighter, relatively difficult to pump He for α capture and H_2 for p capture. Expected transmission probabilities can be estimated by assuming that a vacuum of 2×10^{-8} Torr can be achieved and that it consists of 90 % of such low Z material and the remaining 10% of high Z material such as, N_2, O_2, H_2O, CO_2, and CO, for which the cross sections are approximated as the average of the O_2 and N_2 values shown in Table 4.1.

4.2 Truncated Rutherford scattering

Since it turns out that the unwanted transmission through the mass or final slits of full energy beam ions is not greatly affected by scattering off residual gas atoms through

Table 4.1: Cross section estimates($Angstrom^2$) for some residual gases
Data;
W - Wu et al
M - Macdonald et al (extrapolated to 2.4 MeV)
Empirical expressions;
S - Schlachter et al
A - Alton et al

Proj.	Event:	$q_i \rightarrow q_f$	He	H_2	N_2	O_2	Ar
^{15}O	loss	$3^+ \rightarrow 4^+$	$.3^M(.86^A)$	1.5^A	$1^M(1.5^A)$	1.55^A	$1^M(1.04^A)$
		$4^+ \rightarrow 5^+$	$.1^M(.3^A)$	$.5^A$	$.5^M$	$.53^A$	$.7^M(.6^A)$
		$4^+ \rightarrow 6^+$	$.002^M$	-	$.05^M$	-	$.06^M$
	pickup	$4^+ \rightarrow 3^+$	$1^W(1.2^S)$	$.8^S$	6.3^S	5.9^S	1.04^S
		$5^+ \rightarrow 4^+$	$4^W(1.9^S)$	1.5^S	8.34^S	7.5^S	1.18^S
		$6^+ \rightarrow 4^+$	$.1^W(.1^M)$	-	$.1^M$	-	$.1^M$
^{21}Na		$5^+ \rightarrow 6^+$	-	.49	.8	.83	.55
		$6^+ \rightarrow 5^+$	-	2.46	12	10.6	1.6
^{25}Al	loss	$8^+ \rightarrow 9^+$	-	.088	.14	.15	.1
	p.u.	$9^+ \rightarrow 8^+$	-	.16	3.93	4.32	1.39

very small (< 2 mrad) or large (≥ 30 mrad) angle events we can ignore screening due to electrons and use the bare Coulomb potential Rutherford cross section in the small angle approximation, generating no scattering events below a minimum angle of θ_{min} or above a maximum of θ_{max}. The same 'truncated' Rutherford scattering approach has been used by [9] to Monte Carlo multiple scattering. In the small angle approximation the differential cross section for scattering of an ion of charge state Q off a residual gas atom, inversely proportional to the fourth power of the centre of mass scattering angle, θ,

$$\frac{d\sigma}{d\Omega} = \frac{D^2}{4}[\theta/2]^{-4},$$

where collision diameter, D, is given by

$$D = \frac{Z_Q Z_{resid.} e^2}{\mu v_Q^2},$$

μ is the reduced mass and v_Q ,the relative speed, is taken to be equal to average lab velocity of the ions. The integrated cross section over the range $\theta_{min} < \theta < \theta_{max}$ may be written for $\theta_{min} \ll \theta_{max}$

$$\frac{\pi D^2}{\theta_{min}^2} = \left[\frac{Z_Q Z_{resid.}\,(A_Q/A_{resid.}+1)}{E_Q^{lab}(MeV)}\right]^2 \; 1.63\, Mbarn.$$

A random variable, $0 \leq \Re \leq 1$, is generated that represents the probability of scattering through an angle less than θ,

$$\Re = \frac{\int_{\theta_{min}}^{\theta} [\theta'/2]^{-3} d\theta'}{\int_{\theta_{min}}^{\theta_{max}} [\theta'/2]^{-3} d\theta'}.$$

Solving for the centre of mass angle,

$$\theta = \frac{\theta_{min}}{\sqrt{1 - \Re(1 - (\frac{\theta_{min}}{\theta_{max}})^2)}} \overset{\theta_{min} \ll \theta_{max}}{\simeq} \frac{\theta_{min}}{\sqrt{1 - \Re}}.$$

In the Thomas-Fermi approximation, the bare Coulomb potential is exponentially screened, the differential cross section becoming in the small angle approximation

$$\frac{d\sigma}{d\Omega} = \frac{D^2}{4}[(\theta/2)^2 + (\theta_{scr}/2)^2]^{-2},$$

where the screening angle is defined to be $\theta_{scr} = 1/k_Q a_{scr}$ and k_Q is the ion wavenumber [11]. The screening length, a_{scr}, can be approximated by

$$a_{scr} = \frac{a_B}{\sqrt{(Z_Q(1 - Q/Z_Q))^{2/3} + Z_{resid.}^{2/3}}},$$

where a_B is the Bohr radius. As an example, consider the scattering of E_{lab}=11.72 MeV ^{25}Al off residual ^{14}N atoms. The screening angle, θ_{scr}, is only .01 mrad and the integrated cross section for scattering through centre of mass angles between 1 and 80 mrad is 7.4 (10^{-21}) cm^2.

4.3 Transmission probabilities

Probabilities per unit length, T(z), of the transmission of beam particles through either mass and final slits due to CCC events were determined from RAYTRACE simulations at a number of different longitudinal positions, z, over the region of length L for which transmission was appreciable. Estimates of transmission probabilities due to CCC events are made using effective lengths defined as

$$L_{eff} = \int_0^L T(z)\, dz.$$

Calculations of overall transmission probability due to N successive CCC events occurring along the EMS then take the form,

$$Prob = \left(32 \times 10^{16}\right)^N \sum_{j=1}^{M} \left[\prod_{i=1}^{N} \sigma_{ij}(cm^2) L_{eff}^i(cm) P_{ij}(Torr)\right],$$

where the value 32×10^{16} per cc-Torr corresponds to T = 300 K, P_{ij} is the partial pressure of the jth residual gas and σ_{ij} the corresponding cross section.

Figure 4.1 shows the longitudinal position dependence of the transmission of ^{25}Al beam, expressed as %/Torr-m of ^{25}Al beam being Rutherford scattered by residual N_2 gas so as to pass through the mass slits. The initial beam conditions were the same as for the transmission simulations.

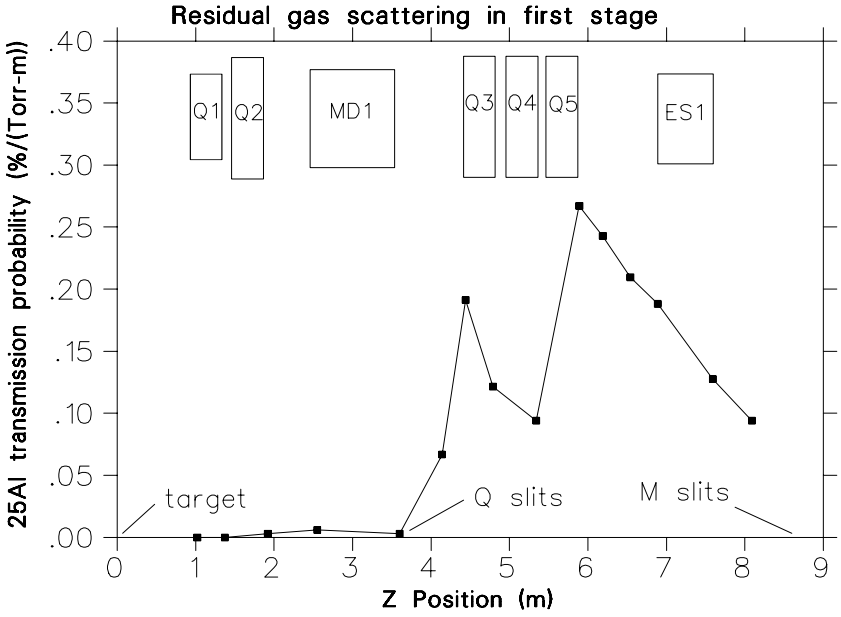

Figure 4.1: Monte Carlo determination of the probability, for ^{25}Al beam of nominal energy 11.75 MeV, to pass through the mass slits after having Rutherford scattered off a N_2 molecule at the position z. For a uniform partial pressure of 10^{-7} Torr N_2, the total area of 0.7 % Torr^{-1} gives a probability of 7×10^{-7} for beam entering the separator to pass the mass slits by Rutherford scattering.

Beam particles scattered so as to pass through the mass selection slits, if unscattered in the second stage of the EMS, would strike the final slits 5 cm from the centre. Thus a second scattering, after the mass slits, would be required to cause transmission of beam through the final slits.

We have simulated Rutherford scattering at a point 5 cm downstream from the exit EFB of Q5 and the subsequent loss of an electron, taking place in a L_{eff}= 10 cm long region centred on the plane normal to the optical axis located at z=98 cm into ED_2. A projection of the trajectories of the ^{25}Al ions onto X-Z and Y-Z planes are shown in Figure 4.2.

The 1 % of the Q=8 ^{25}Al that pass through the M slits translates into a probability "density" of 0.25 %/Torr-m, corresponding to the maximum in Figure 4.1. As an estimate of the combined probability with which the resulting Q=9 ^{25}Al ions pass

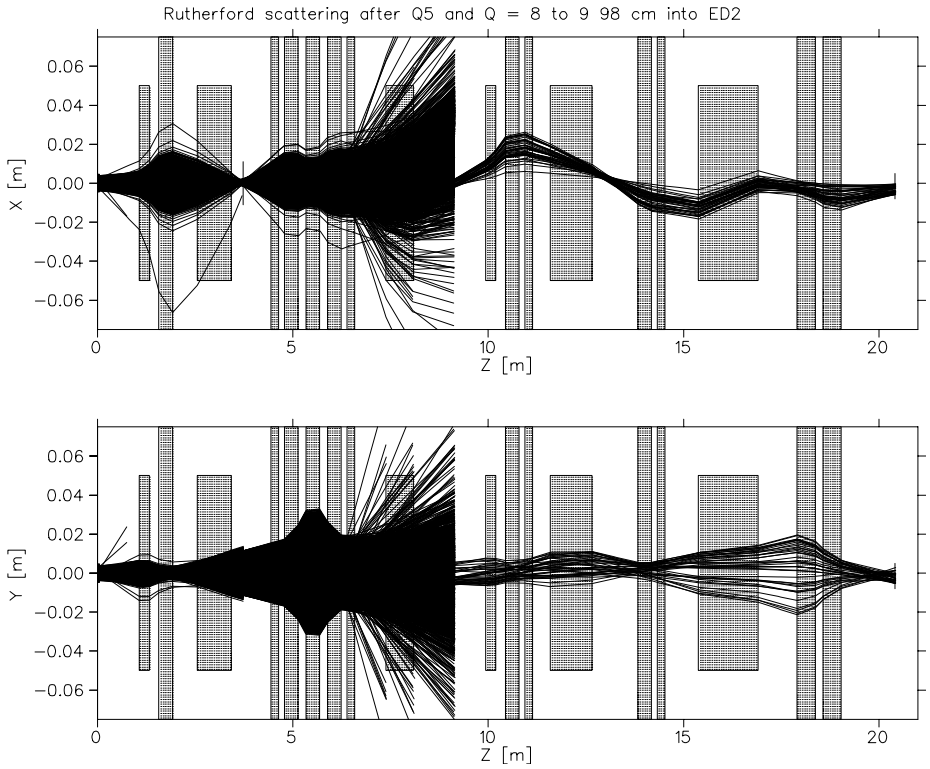

Figure 4.2: Simulation of Rutherford scattering of Q=8 ^{25}Al in the first stage followed by single electron loss in ED_2. Projections of the trajectories onto X-Z and Y-Z planes are shown.

through the F slits we assume it is reasonable to take the integral of Figure 4.1 as the probability of passing through the M slits and that the residual gas throughout the first stage and in ED_2 has a partial pressure of N_2 of 5 10^{-8} Torr. Under these assumptions the combined probability, $P_{tot} = P_{RutherfordthruM} P_{CCCthruF} = (3.5 \times 10^{-7})(2.3 \times 10^{-6}) = 7.5 \times 10^{-13}$ which would constitute a background about half as intense as the ^{26}Si product.

4.4 Shotgun simulations

The next stage of simulation was to introduce tails in the distributions of beam energy and angle, such as might be produced by slit scattering in the target pumping apertures or by scattering from gas or walls in the region downstream of the gas target but before the charge slits. Once again the Q=8 ^{25}Al case was considered since differences between beam and product rigidities are minimal for this reaction. This first "shotgun" simulation started by assuming that ^{25}Al beam particles uniformly filled an acceptance defined by the opening at the charge-selection slits, a ±24 mrad range in angles, and

energies between 95 and 105 % of nominal product energy. Subsequent simulations allowed the range of initial positions, angles and energies of the ions that constituted the part of the "tail" that came closest to passing through the final slits to be identified. None of the events generated passes closer than 2.4 cm from the nearest final slit edge. The initial phase space regions and the positions in the final focal plane, X_F, of these "most intrepid" ions versus their energies are shown in Figure 4.3.

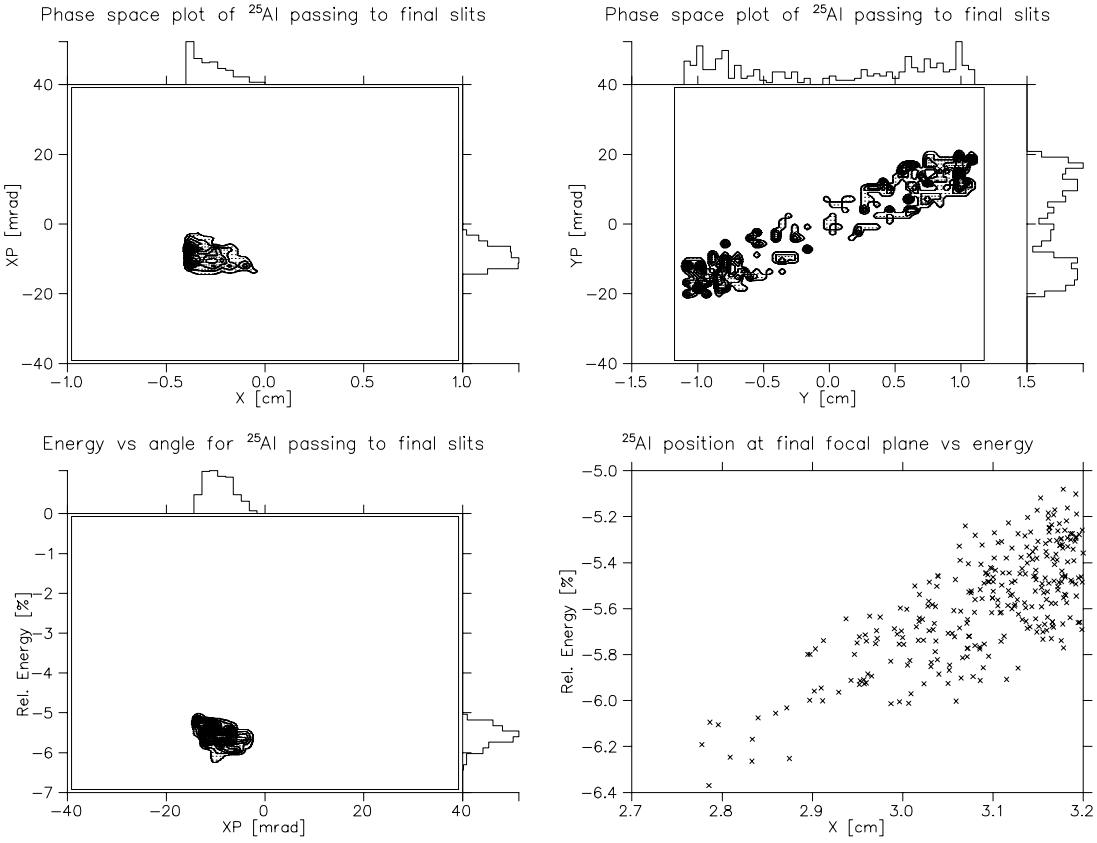

Figure 4.3: Plots of initial phase spaces of Q=8 ^{25}Al that approach most closely to the final slits, X_Q vs. X'_Q, Y_Q vs. Y'_Q and the energy-X_Q correlation, as well as the correlation of their positions in the final focal plane, X_F, with their energies.

Some further change in direction or rigidity would be needed to have these particles pass through the final slits. There remains the question of estimating the strength of background which might be found within the "shotgun" acceptance. Estimates of the fraction of incident beam in the low-energy or large-angle tails can be little more than educated guesses until the accelerators are built and beams extracted from them. However, estimates can be made for the probability that beam is scattered by the gas target onto a solid surface, then re-scattered into the acceptance of the separator. For smooth surfaces at larger angles of incidence, "reflection" arises from single large-

angle scattering rather than multiple scattering, and the probability drops rapidly as the angle increases. For 2.4 MeV ^{15}O ions hitting a smooth Fe surface at 20 mrad, approximately 2% could be reflected with energy loss of 5% or less into a solid angle of (40 mrad)^2. The probability drops markedly as the atomic number of the material decreases – reflecting the rapid change in ratio of Rutherford scattering cross section to dE/dx.

An estimate of background of the "shotgun" pattern is obtained by observing that GEANT estimates approximately 0.1% of the ^{15}O beam would be scattered onto the downstream pumping tubes. Implemented as a series of thin apertures, the pumping tubes should present an oblique surface to not more than 10% of such scattered beam and the oblique scatterings should result in less than a few per cent scattered into the acceptance of the "shotgun" distribution at the charge slits. With further suppression of this background by the mass slits, we can plausibly estimate that the first stage of the separator will provide suppression of better than 10^6 for this type of background.

Chapter 5

Field strength stability and uniformity requirements

5.1 Summary of requirements

Field stability requirements have been studied using RAYTRACE simulations and the following values are suggested;

- *quads and sextupoles* ± 0.1 %
- *XY steerer magnets* ± 0.5 % (???)
- *electric dipole fields(voltages)* $\pm 0.05(0.025)$ %
- *magnetic dipole fields* ± 0.025 %

Field uniformity requirements for magnetic and electric dipoles are described in more detail below.

5.2 Field stability requirements

5.2.1 Quads and sextupoles field stability requirements

The required quad field strength stabilities have been estimated by calculating the percent change in strength of each one of the quads taken separately that results in a reduction of ^{19}Ne transmission by about 2 % (from a nominal value of 94.4 %). The results of this calculation are shown in figure 5.1. The most sensitive setting is that of Q2 for which a .25 % change in field strength increases the transmission of ^{19}Ne by 2 %. A stability of ± 0.1 % should ensure that there are no important variations in recoil product transmission.

Transmissions of recoil product are relatively insensitive to the sextupole settings, however given the possibility of difficult to simulate tails due to aberrations, it is suggested that the stability requirement be the same as for the quads, ± 0.1 %.

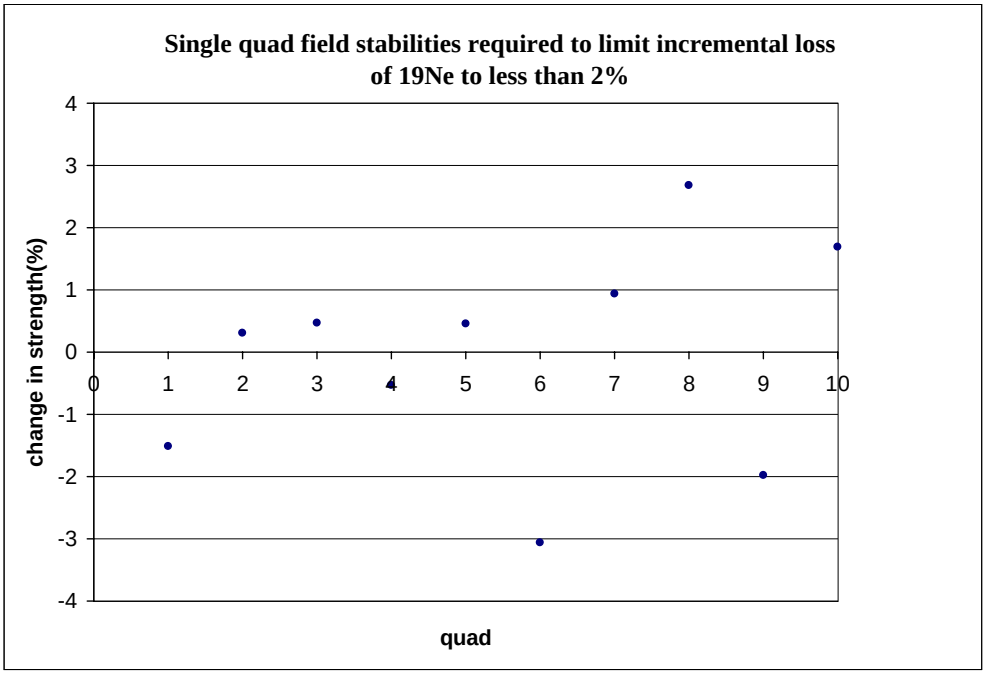

Figure 5.1: Calculated quad field changes that result in an increase in the total loss of ^{19}Ne of about 2 %.

5.2.2 Magnetic and Electric dipole field stability requirements

The required field strength stabilities for the dipoles have been estimated by using RAYTRACE to determine the percent change in strength of each one of the dipoles taken separately that results in an overall reduction of GEANT simulated ^{19}Ne and ^{26}Si transmission of about 2 % (from nominal values of 94%). The Q, M and F slits were set for the unperturbed case so that 1 % of the recoil product are lost on each pair of X and Y slits. The results, shown in Table 5.1, can be understood ias dipole field variations shifting the recoil product distributions horizontally with respect to fixed slits. The worst cases are underbending for the magnetic dipoles and overbending for the electric dipoles. The shifts of the central rays at the M and F slits corresponding to incremental 2 % recoil product loss cases, Δx, are -0.5 and -1.2 mm (i.e. to the right (x<0) viewed along the optical axis). The results for ^{19}Ne and ^{26}Si are identical for variations of MD_1 and ED_1 strengths, stabilities of $\pm$0.1 % for ED_1 and $\pm$0.05 % for MD_1 ensuring that the incremental loss for a given variation is less than 2 %. However in the more highly dispersive second stage, due to the uncorrected (x$|\delta_E\delta_E$) aberration, the distribution of product at the F slits are broader the larger the recoil cone. The distribution of ^{26}Si for example, because it falls off more sharply than that of ^{19}Ne requires that the stability of MD_2 and ED_2 fields be about twice as good.

Table 5.1: Results of stability simulations for electric(E) and magnetic(B) dipole fields. Incremental losses are for ^{19}Ne except for the entries after "/" which are for ^{26}Si.

Dipole	$\frac{\Delta B}{B}$ or $\frac{\Delta E}{E}$ (%)	Incremental loss (%)			
		Q	M	F	Tot.
MD_1	.15	-1.4	0.9	-1.6	-2.1
	-.05	0.3	-1.9	-0.2	-2.0
ED_1	.1	-	-1.6	-0.2	-1.8
	-.3	-	0.8	-2.2	-1.8
MD_2	.08	-	-	-2.2	-2.3
	-.05/-.025	-	-	-2.4/-1.6	-2.4/-1.6
ED_2	.1/.05	-	-	-1.8/-1.6	-1.8/1.6
	-.15	-	-	-2.3	-2.3

Adopting stability requirements for magnetic and electric fields of $\pm$0.025 and $\pm$0.05 % respectively will restrict incremental losses due to a given dipole to 2 %. This should be attainable using constant current supplies stable to $\pm$0.01 % and NMR controllers placed in a sufficiently uniform field region (note that for the low rigidity ^{19}Ne tune $\pm$0.025 corresponds to $\pm$0.5 G for the $\sim$2 kG MD_1 field). To maintain the electric field tolerance it will be necessary to maintain both anode and cathode voltages to within $\pm$0.025 %. It remains to note that the ^{15}O beam exiting ED_1 is moved out towards the outer electrode by only $\frac{\Delta E}{E}\ \rho_{^{15}O} = .0005(200)19/15 = 0.127$ cm when the field is

reduced by 0.05 %. This should not result in a large increase in the amount of ^{15}O striking the outer electrode there, a part of which may scatter off the electrode end and pass through the mass slits.

5.3 Magnetic and Electric Dipole uniformity tolerances

For the magnetic and electric dipoles misalignment of the poles/electrodes results in non-uniform field distributions. There are two questions that arise;

- have we correctly described the fields and
- what are the gap and electrode misalignment tolerances?

Experience with RAYTRACE has shown that it is capable of describing real field distributions for magnetic dipoles and it has been used to simulate the effect of field non-uniformities on recoil product transmission. See the discussions below for details on how we arrived at tolerances. Simulations with misaligned electrodes were not made for the electric dipoles.

5.3.1 Magnetic dipole field uniformity

We have investigated the sensitivity of the DRAGON separator tunes to non-uniformities in the fields of MD_1 and MD_2. The method was to use RAYTRACE to study transmission of 1000 recoil ions representative of a large-emittance reaction. Software slits were set in x and y at the Q, M, and F locations and adjusted so that each x-y pair cut out not more than 1 to 1.5% of the ions. Non-uniformities were then turned on in the RAYTRACE description of the uniform-field regions of MD_1, MD_2 until losses increased by an additional 1%. The RAYTRACE parametrization of non-uniformity in the dipoles is:

$$B(r) = B_o \left[1 - n\left(\frac{r}{R}\right) + BETA\left(\frac{r}{R}\right)^2 + GAMMA\left(\frac{r}{R}\right)^3 + DELTA\left(\frac{r}{R}\right)^4 \right] \quad (5.1)$$

The results are shown in table 5.2.

The linear term (index n) corresponding to non-parallel poles is asymmetric: we are much more sensitive to negative n ("anti-clamshell") than to deviations in the sense of a normal clamshell dipole. The quadratic and quartic terms (BETA,DELTA) we would expect to arise from finite pole widths.

The numbers in table 5.3 are amounts by which the field may decrease relative to the central value.

It is specified that the gaps be uniform to within ±.002 inch. George Clark has performed OPERA3D and OPERA2D field calculations for MD_1(see TRI-DN-98-12) and MD_2(see TRI-DN-98-10) respectively. He considered the worst case of pole pieces

Table 5.2: Results of magnetic dipole uniformity simulations

			losses per 1000 ions at					
Magnet	RAYTRACE param.		Q_x	Q_y	M_x	M_y	F_x	F_y
MD_1	none	-	9	6	8	8	9	7
	n	-0.01	10	6	11	8	12	7
	BETA	-0.5	9	5	14	9	12	6
	DELTA	-400.	9	5	14	9	10	6
MD_2	none	-	-	-	-	-	9	7
	n	-0.005	-	-	-	-	15	7
	BETA	-0.2	-	-	-	-	15	7
	DELTA	-50.	-	-	-	-	15	7

Table 5.3: Suggested field uniformity specifications for magnetic dipoles.

	MD_1	MD_2
uniform region width(mm)	±60	±60
bending radius (mm)	1000	813
(r/R)	0.060	0.0738
uniformity spec. from:		
n	-0.06%	-0.04%
BETA	-0.18%	-0.11%
DELTA	-0.5%	-0.14%

being non-parallel, the gaps on the inside and outside of the bending direction being .002 inch larger and smaller than the design values respectively(i.e. "anti-clamshell"). Fitting the results to the above RAYTRACE expression he finds values that are much smaller than those shown in table 5.2. Over the uniformity regions specified in table 5.3 he finds field uniformities that are superior to 0.1%. In practice the effective lengths will depend strongly on the length of the steel (maufacturing tolerance of ±0.01 inch) and such details as the size and placement of the coils. These inevitable differences from the design values quoted above will be compensated for by adjusting the field strengths accordingly. There is little or no difference in the transmission of ^{19}Ne for changes in the effective lengths of up to ±1% compensated in this way.

5.3.2 Electric dipole field uniformity and misalignments

Bruce Milton has carried out a study that uses Poisson 2D calculations to arrive at the final choices for the geometry of the electrodes, the shrouds shielding the rib structure that supports the electrodes and the field clamps. He was able to verify that effective field boundaries are normal to the optical axis and that RAYTRACE adequately

describes the resulting field distributions(see TRI-DN-98-14 for details).

The most important consideration is that the integrated field experienced by particles at a given radius of curvature should not vary by more than 0.1% within the central ±40 mm above and below the median plane of ED_1 or the central ±50 mm of ED_2. This ensures that the deflection of particles at the following achromatic focus shall be the same for different heights of trajectory, to within 10% of the expected spot size at the focus. Accordingly, the average gap between electrodes must be uniform to within 0.1% or 0.1mm, as a function of height, within the "high field-uniformity" regions. Local variations in excess of 0.1mm may be tolerated provided they are smooth and are of a random nature such as to cancel over the length of the dipole.

For the electric dipoles the falloff of field vertically from its midplane value dictates how tall the electrodes must be. We calculate the vertical falloff using the analytical expression for semi-infinite parallel plates but there is no provision to include the result in RAYTRACE. In this case we insist that the electrodes of ED_1 and ED_2 be tall enough so that no ^{19}Ne ion trajectories in the RAYTRACE simulation pass between the electrodes at vertical distances from the midplane that exceed the point at which the above calculation predicts a 0.1 % droop from the central field value.

In the fringing field regions the situation becomes fully 3D and there was some concern that we might be neglecting an effect that will translate into a height dependent effective length over the above "high uniformity" region. In order to verify this Bruce Milton performed a 3D TOSCA calculation with realistic dimensions including; end and edge radii, shrouds and a field clamp (the y=0 dimensions correspond to the 'offset' case in TRI-DN-98-14). He determined the y dependence of the effective field boundary position, Z, in the x=0 plane to be,

$$\frac{\Delta Z}{Z}(\%) = -.165\left(\frac{y}{width}\right)^2 - .45\left(\frac{y}{width}\right)^4, \tag{5.2}$$

and the vertical falloff of the electric field strength to be,

$$B(y) = \frac{B(0)}{1 + exp\left[-1.5 + 6.5\left(\frac{y-width}{gap}\right)\right]}, \tag{5.3}$$

where width = 15 cm is the half height of the electrodes and gap = 10 cm. Combining these expressions he calculated the fractional decrease in the effective length with distance from the median plane. The effective length decreases from the central value by 0.1 % about 5.5 cm from the median plane.

Misalignments of the electrodes are treated qualitatively by Boerboom [1]. He considers image aberrations in an imperfectly-shaped electrostatic analyser. He considers cylindrical electrodes having radii of curvature much larger than the gap between them, which in turn is much larger than their deviations from ideal geometry. Boerboom applies his formalism to examples of misaligned electrodes which are of interest for DRAGON design:

1. inner and outer electrodes have correct radii of curvature, but axis of outer electrode is shifted with respect to rotation axis of the inner electrode. Result is that

the focussing is not influenced and only a shift of the image results. This could be remedied by a small adjustment in electrode voltages.

2. deformed outer (or inner) electrode. If the electrode is not exactly circular but can be approximated by an ellipse, again the result is that the focus is shifted but not otherwise worsened.

3. non-parallel: electrodes not exactly perpendicular to the median plane. The image, instead of being upright and sharp, becomes tilted and unsharp.

4. conical electrodes. Again, in general, an oblique unsharp image results.

5. toroidal electrodes. Extra terms are of higher order and very small.

We can consider the case of non-parallel cylinders as applied to the DRAGON ED_1 dipole. Assume the inner and outer electrodes are each tilted with respect to the vertical by a small angle v such that the gap (G) at a height y above the median plane is reduced by a factor (1+ 2vy/G). The tune calls for the average vertical envelope in ED_1 to be not more than ±2 cm, so a misalignment by v=0.001 radian would produce a change in gap (and thus in electric field strength) of not more than 2vy/G = 2x2x0.001/10 = ±0.04%. The dispersion at the mass slits is 0.45 cm/%, so the result of a ±1 mrad electrode misalignment should be approximately ±0.018 cm worsening of the image. This is to be compared with an expected image size of order ±0.25 cm. A vertical misalignment will result also in vertical components of electric field E, increasing from 0 at the central radius to vE at an electrode surface. At an average orbit envelope of x=3 cm, the unwanted component of vertical deflection will amount to 0.001 x 3/5 of the total deflection by 20 degrees or 0.35 radians. The result is of order ±0.2 mrad. We would expect that at the M slits the unwanted vertical deflection would be approximately 0.025 cm (added to more than ±1 cm envelope). Note the sense of the deviations produced by the non-parallelism: orbits near x=0 will be over-deflected in horizontal angle when y is in the direction of narrowing gap and underdeflected for the opposite values of y; orbits near y=0 will be deflected up or down by an amount proportional to x. At the exit of the misaligned dipole the directions of off-axis orbits will be deflected relative to the ideal case in the same sense as for a quadrupole rotated by 45 degrees. This is no doubt the origin of a comment made by H. Wollnik to J. D'Auria about adding a small quad rotated by 45 degrees, to correct for electrostatic dipole alignment problems.

A criterion of keeping alignment aberrations to less than 10% of expected image size would allow a vertical misalignment of slightly more than 1 mrad by each electrode relative to the vertical. It should be noted that the requirement is to be met in the region where the orbits pass, the 2 cm closest to the median plane of ED_1.

In ED_2 the tune calls for a vertical envelope averaging as much as ±4 cm, leading to double the relative spread in horizontal deflection (0.08%) from a 1 mrad misalignment. An F-slit dispersion of about 1.3 cm/% due to ED_2 means an additional ±0.1cm spread (out of approximately ±0.8 cm GIOS-estimated aberrations). The horizontal

extent of product in ED_2 is not much different on average from that in ED_1 but its larger deflection (35 degrees vs 20 degrees) means approximately ± 0.35 mrad unwanted vertical deflection after ED_2 from a 1 mrad misalignment. Again, the expected effect at the F slits is less than 10% of the calculated spot size.

Chapter 6

Misalignment of Quads and sextupoles; tolerances and corrections

Knowledge of the accuracy to which each of the optical elements must be positioned in order to assure that there is no significant reduction in performance due to misalignments is necessary. For quadrupoles and sextupoles, if identical poles and coils were symmetrically placed, optical axes would coincide with symmetry axes. In practice careful field mapping will allow the position of the ion optical axes to be determined to the desired accuracy. Acceptable tolerances are those that do not affect transmission or which correspond to misalignments that can be corrected by adjusting dipole strengths and the vertical and horizontal steerers ST1, ST2, ST3 and ST4 (see figure 1.1).

Below we begin by discussing the effect of misalignments on the performance of the separator and then consider how to use steering and dipole field adjustments to recover, as near as possible, the unperturbed performance. We consider ^{19}Ne transmission since, due to the relatively large energy and angle spread of the recoils, alignment of the optical axes with the magnetic centres of the aberration correcting sextupoles is most critical in this case.

The conclusion is that nearly all misalignments corresponding to positioning errors of $\sim$1 mm can be corrected by using small changes in dipole strengths and the four steerer magnets ST1, ST2, ST3 and ST4 to aim for the centres of the next downstream beam position monitor. It has been found that the exceptional case of vertical misteering in the first doublet can be handled by placing a compact XY steerer (labelled ST0 below) immediately after the last downstream collimator box. This capability is important due to the necessity of passing through the magnetic centre of Q2 which will have pole pieces shaped to produce a sextupolar pole tip field 5 to 6 % the quadrupole value.

6.0.3 Calculation of misalignments

The effect of changes in the position and orientation of each pole (i.e. quadrupole or sextupole) on the transmission of ^{19}Ne through the separator has been studied using RAYTRACE. The reference frame used has x pointing to the left when viewed along the beam axis z. Shifts along and rotations about these axes are considered separately for the pole in question, the other poles being aligned ideally. Transmissions were calculated from 1000 initial ^{19}Ne ion trajectories, generated using the GEANT simulation described in the MIG. Plots of changes in the transmission through the charge(Q), mass(M) and final(F) slits are shown in Figures 6.8 to 6.19 below. The vertical scales indicate percent changes in ^{19}Ne losses relative to the unperturbed values for each of the Q, M and F slits, 1.4, 2.3 and .7 % respectively. The horizontal scale indicates which of the poles was perturbed, 1 to 14 corresponding in order to Q1, Q2, S1, Q3, Q4, Q5, S2, Q6, Q7, S3, Q8, S4, Q9 and Q10. Shifts of both $\pm$ 1 and 2 mm were considered in each of the horizontal(x), vertical(y) and longitudinal(z) directions. Rotations about each of the x, y and z directions of $\pm$ .1 and .5 degrees were also considered. Rotations are applied at entrance effective field boundaries. Positive rotations are clockwise viewed along the axis in question. In general, transverse shifts of a focusing(defocusing) quad in a given direction results in steering in the same(opposite) direction. The effect of a quad or sextupole rotation about a given axis at the entrance effective field boundary is equivalent to a translation of the exit boundary in the orthogonal plane to it(see Figures 6.5 and 6.6 for examples).

The effect of longitudinal shifts are only expected to be important when the shift is large compared to the distance from the quad to the image.

6.0.4 Correction of misalignments

There are 4 identical, combination horizontal/vertical steerers with 6.25 inch gaps and effective lengths of 37 cm. Adjustment of dipole field strengths provides additional horizontal steering. Vertically, only steerers may be used to correct for misalignments. The adjustment of steerers and/or dipole strengths is accomplished sequentially. This is illustrated below in detail for the specific case of a shift to the left of Q2 by 1mm. The basic idea is to use a steering device to aim for the centre of the next downstream location at which a centroid may be determined. These locations include the Q, M and F slits and 4 beam monitor locations indicated in Figure 1.1 by the prefix MON. Centroids are calculated using ^{19}Ne ions with the same emittance as the beam. In practice this would be an intense, probably stable pilot beam. Each choice of steerer or dipole strength that centres the pilot beam in the next slit or beam monitor downstream is determined iteratively in 2 to 3 steps. This procedure, outlined in the Appendix, could be easily incorporated into RAYTRACE. Also in the Appendix is the RAYTRACE input file used.Once the pilot beam has been centred at each position the resulting slit transmissions are calculated. It was found that

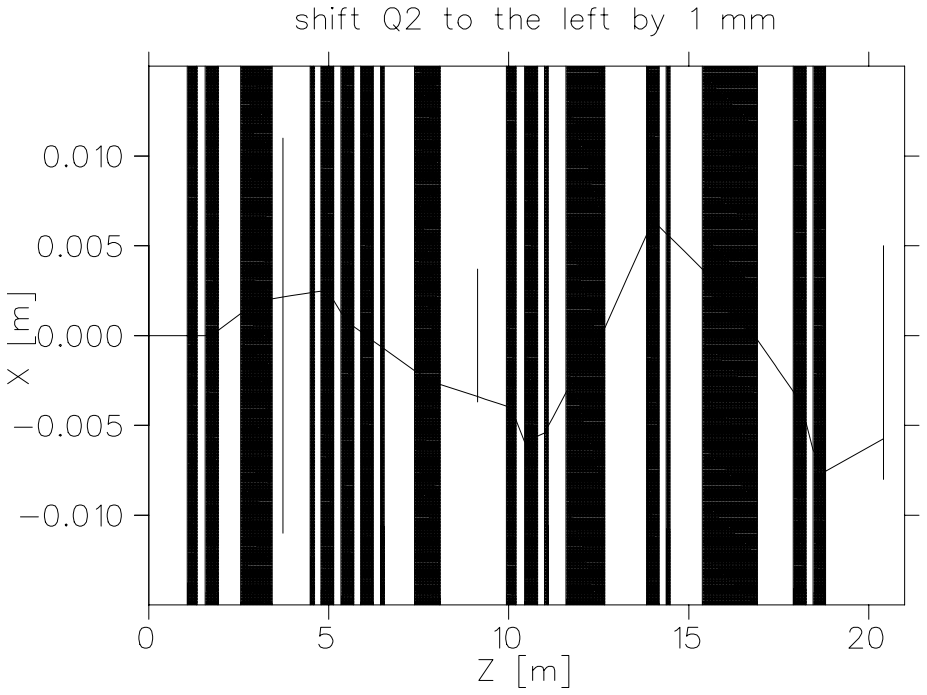

Figure 6.1: New central ray with Q2 shifted to the left by 1 mm.

6.1 Horizontal shifts and rotations about the vertical axis

6.1.1 Discussion of misalignments

As may be seen from the transmission figures, shifts of Q2, Q4 and Q7 by 1 mm (or to the left as viewed along the beam axis) result in large losses at the mass and final slits. Consider the shift of Q2 to the left by 1 mm (see ^{19}Ne loss calculation change Figure 6.8). The calculated transmission data can be understood as resulting from displacements of the ion optical axis at the slit locations. As may be seen in figure 6.1 which plots the trajectory of the central ray, the bend to the left following Q2 causes Q3 to steer ^{19}Ne strongly to the right resulting in a loss at the mass slits of about 45%. Loss at the final slits due to a shift of Q7 is analogous. The loss at the mass slits due to a shift to the left of Q4 by 1 mm, which unlike Q2 and Q7 is defocusing in the horizontal, bends the axis to the left as illustrated in Figure 6.2, resulting in large and small losses at the mass and final slits respectively when compared with the other 2 focussing quads making up the triplet, Q3 and Q4. The corresponding plots of the new central ray trajectories for shifts of Q3 to the left and right by 1 mm are shown for comparison in Figures 6.3 and6.4.

The fact that no appreciable change in ^{19}Ne slit loss is seen for x and y shifts for sextupoles (pole numbers 3, 7, 10 and 12 in Figures below), can be understood as follows. Since the distribution of recoils in sextupoles is wide and short by design,

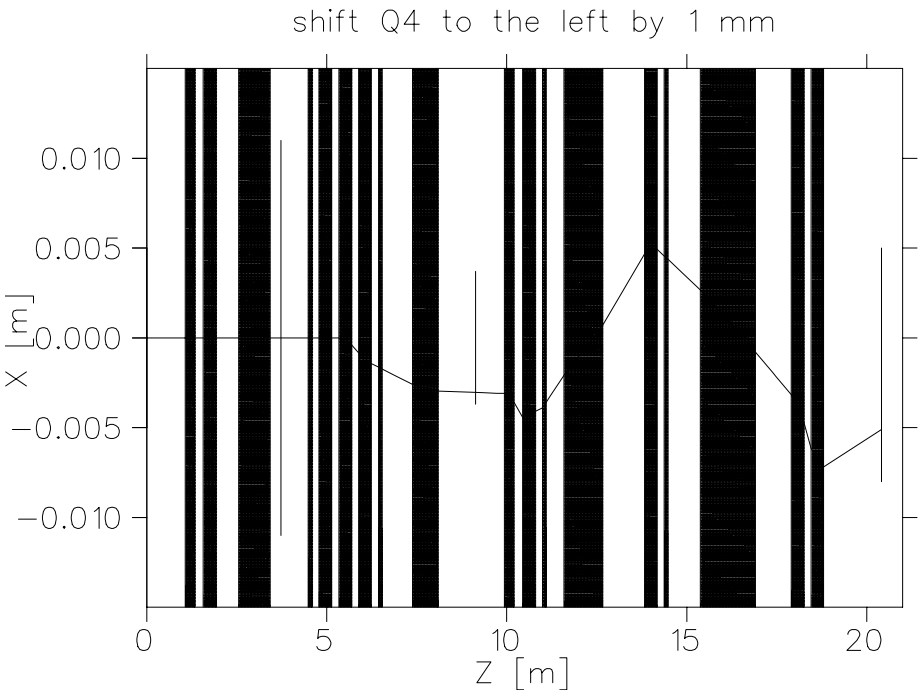

Figure 6.2: New central ray with Q4 shifted to the left by 1 mm.

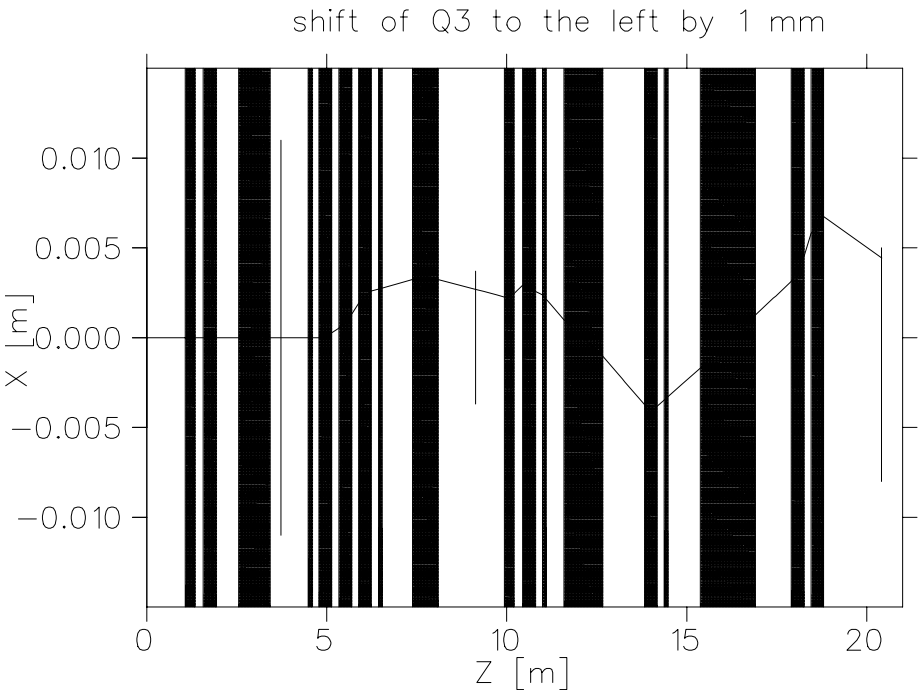

Figure 6.3: New central ray with Q2 shifted to the left by 1 mm.

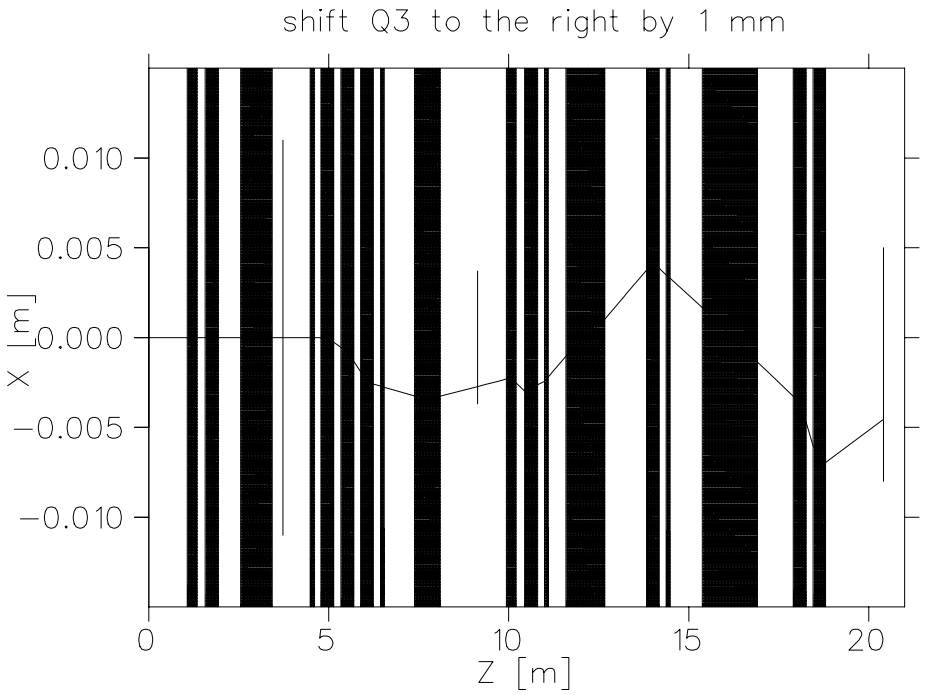

Figure 6.4: New central ray with Q2 shifted to the right by 1 mm.

their motion is dominated by the veritical field near the horizontal midplane, which increases quadratically with the distance from the centre. For equal placement errors, x_0, the ratio of unwanted steering to the desired field, $(x_0/x)^2$ for a sextupole, is much smaller than the (x_0/x) quadrupole value. The only significant effect is observed for S1 for a rotation about the vertical(see Figure 6.6).

6.1.2 Correction of misalignments

In all the cases considered, non perturbed ^{19}Ne slit transmissions can be recovered by using horizontal steerers and adjusting dipole fields appropriately. Two tables summarize, for the most sensitive quads, total ^{19}Ne transmissions before and after correction, along with the steerer and dipole settings used; Table 6.1 for shifts in x and Table 6.4 for rotations about the y axis.

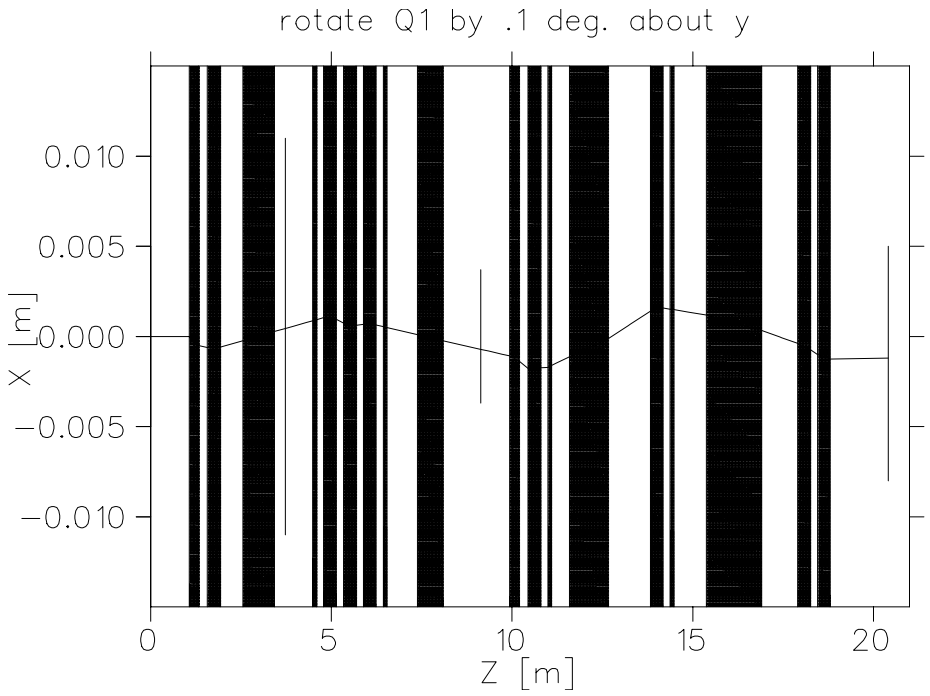

Figure 6.5: New central ray with Q1 rotated about y by .1 deg..

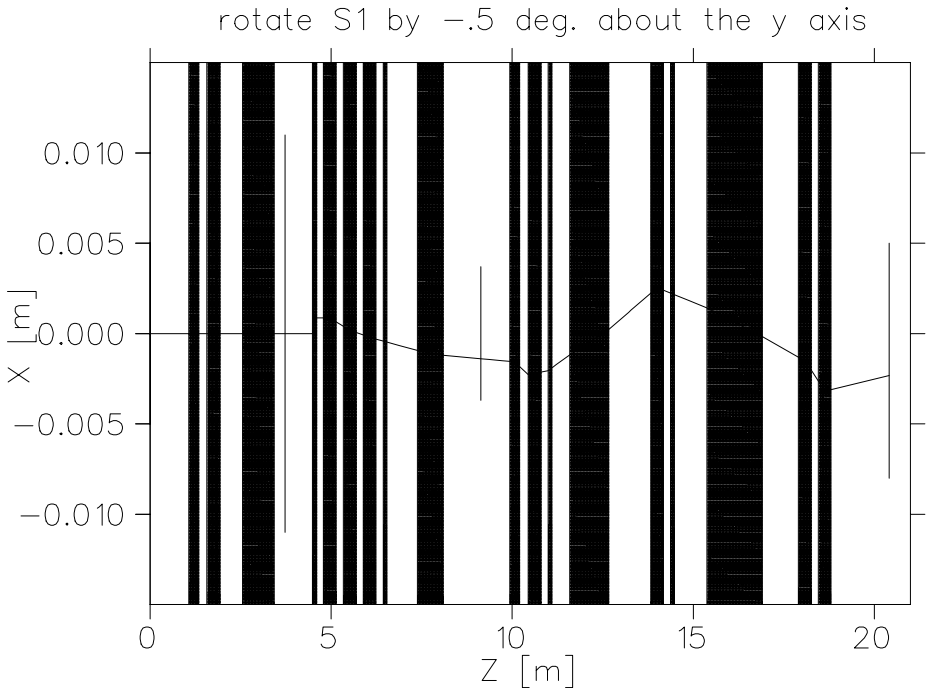

Figure 6.6: New central ray with S1 rotated about y by .5 deg..

Table 6.1: Summary of Horizontal Quad Shifts and Corrections

				Steerer Settings							
Quad	Shift	^{19}Ne *Loss* (%)		MD_1	ST1	ED_1	ST2	MD_2	ST3	ED_2	ST4
	(mm)	uncorr.	corr.	$\frac{\Delta B}{B}$(%)	(mT)	$\frac{\Delta V}{V}$(%)	(mT)	$\frac{\Delta B}{B}$(%)	(mT)	$\frac{\Delta V}{V}$(%)	(mT)
-	-	4.4	-	-	-	-	-	-	-	-	-
Q1	+1	9.1	4.4	-0.195	1.06	-0.242	-	-	-	-	-
Q1	-1	19.5	5.2	0.194	-1.14	0.166	-	-	-	-	-
Q1	+2	50.3	4.3	-0.392	2.11	-0.486	-	-	-	-	-
Q1	-2	59.3	6.0	0.387	-2.20	0.405	-	-	-	-	-
Q2	+1	51.9	4.6	0.356	-1.26	0.195	-	-	-	-	-
Q2	-1	43.9	5.1	-0.357	1.18	-0.271	-	-	-	-	-
Q3	+1	25.5	4.5	-	1.15	0.312	-	-	-	-	-
Q3	-1	34.9	5.4	-	-1.24	-0.388	-	-	-	-	-
Q4	+1	43.4	5.7	-	-0.90	-0.531	0.63	-	-	-	-
Q7	+1	26.7	4.9	-	-	-	0.37	0.150	-0.68	-	-
Q7	-1	22.4	5.4	-	-	-	-0.24	-0.173	0.81	-	-
Q10	+1	6.9	4.8	-	-	-	-	-	-	-	0.79
Q10	-1	8.6	4.7	-	-	-	-	-	-	-	-0.72

Table 6.2: Summary of Rotations of a Quad about a Vertical Axis and Corrections

				Steerer Settings							
Quad	Rotation	^{19}Ne *Loss* (%)		MD_1	ST1	ED_1	ST2	MD_2	ST3	ED_2	ST4
	(deg)	uncorr.	corr.	$\frac{\Delta B}{B}$(%)	(mT)	$\frac{\Delta V}{V}$(%)	(mT)	$\frac{\Delta B}{B}$(%)	(mT)	$\frac{\Delta V}{V}$(%)	(mT)
-	-	4.4	-	-	-	-	-	-	-	-	-
Q1	+0.5	57.7	4.1	0.369	-0.15	-0.059	-	-	-	-	-
Q1	-0.5	48.2	6.8	-0.372	0.08	-0.019	-	-	-	-	-
Q2	+0.5	40.2	4.3	0.293	-	-	-	-	-	-	-
Q2	-0.5	25.9	5.1	-0.294	-	-	-	-	-	-	-
Q7	+0.5	21.0	4.5	-	-	-	-	0.140	0.16	-0.010	-

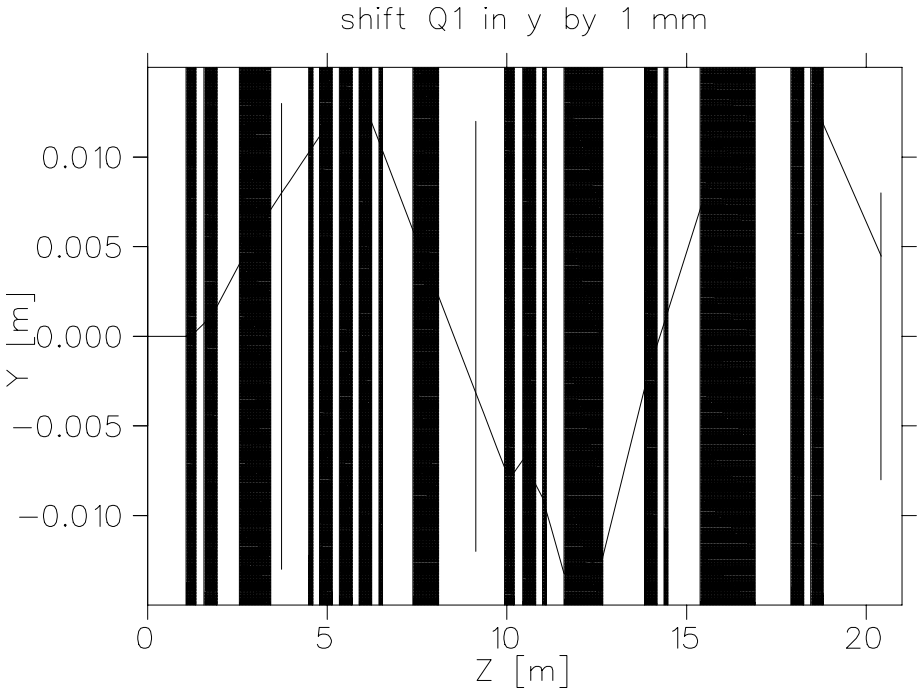

Figure 6.7: New central ray with Q1 shifted in y by 1 mm.

6.2 Vertical shifts and rotations about the horizontal axis

6.2.1 Calculation of misalignments

For shifts, significant increases in ^{19}Ne loss at the slits are seen for Q1, Q4 and Q9, and for rotations at Q2, Q3, Q5 and Q10. As an example, the optical axis for a shift in y of 1 mm for Q1 is shown in Figure 6.7. The transmission depends only slighty on the sign of the shifts and rotations, presumably since there is no dispersion in the vertical plane.

6.2.2 Correction of misalignments

Correction of vertical misteerings, since the dipoles are not useful, is more difficult than for the horizontal case. The situation for Q1 and Q2 may require the placement of vertical steering somewhere upstream. There are plans to temporarily place both vertical and horizontal steerers at the gas target centre during commissioning, in order to be able to explore the entire DRAGON acceptance using low emittance stable beam. Since these massive (return yokes) objects would obstruct gammas a better alternative would be to place a vertical steerer further downstream. For the purposes of this study a vertical steerer with an effective length of 20 cm has been placed 5cm in front of Q1 (EFB to EFB distance).

Table 6.3: Summary of Vertical Quad shifts and Corrections

Quad	Shift (mm)	^{19}Ne *Loss* (%)		Steerer Settings ST0 (mT)	ST1 (mT)	ST2 (mT)	ST3 (mT)	ST4 (mT)
		uncorr.	corr.					
-	-	-	5.2	-	-	-	-	-
Q1	+1	23.5	6.0	2.65	0.076	-	-	-
Q1	-1	23.4	5.8	-2.65	-0.076	-	-	-
Q4	+1	40.2	6.9	-	3.13	1.08	-	-
Q4	-1	39.5	6.5	-	-3.13	-1.08	-	-

Table 6.4: Summary of Rotations of a Quad about a Horizontal Axis and Corrections

Quad	Rotation (deg)	^{19}Ne *Loss* (%)		Steerer Settings ST0 (mT)	ST1 (mT)	ST2 (mT)	ST3 (mT)	ST4 (mT)
		uncorr.	corr.					
-	-	-	5.2	-	-	-	-	-
Q2	+0.5	22.7	6.2	2.54	-0.397	-	-	-
Q2	-0.5	23.6	5.8	-2.54	0.398	-	-	-
Q3	+0.5	35.5	6.6	-	-2.86	-1.39	-	-
Q3	-0.5	35.6	6.5	-	2.86	1.39	-	-
Q5	+0.5	26.4	6.1	-	2.54	0.523	-	-
Q5	-0.5	27.5	5.5	-	-2.54	-0.523	-	-

6.3 Correction algorithm

What follows is a copy of Kris Sigurdson's description of the procedure he used to correct misalignments (from his co-op report, summer 98).

In each case one of the beam components was moved or rotated, and then corrected by observing the propagation of an ion that travels along the optical axis. Such an ion starts at the origin with no initial angle, and has the tuned energy and charge state. The correction procedure is a simple 'method of shooting' one and is outlined in the following;

1. start at the first steering magnet
2. determine the monitor or slit location to center the test ion
3. decide on an acceptable threshold value ϵ
4. record the position value x_0, x_n at the location of interest
5. vary the steerer field strength B_0, B_n by a small amount
   ΔB_0, $\Delta B_n = B_n$ - B_{n-1}
6. observe the new position value x_1, x_{n+1} at the location of interest
7. if $x_1 < \epsilon$, $x_{n+1} < \epsilon$ then goto 8, otherwise
   $B_1 = B_0 + x_1/(x_0 - x_1)*\Delta B_0$
   $B_{n+1} = B_n + x_{n+1}/(x_n - x_{n+1})*\Delta B_n$, let $n \rightarrow n+1$ and goto 6

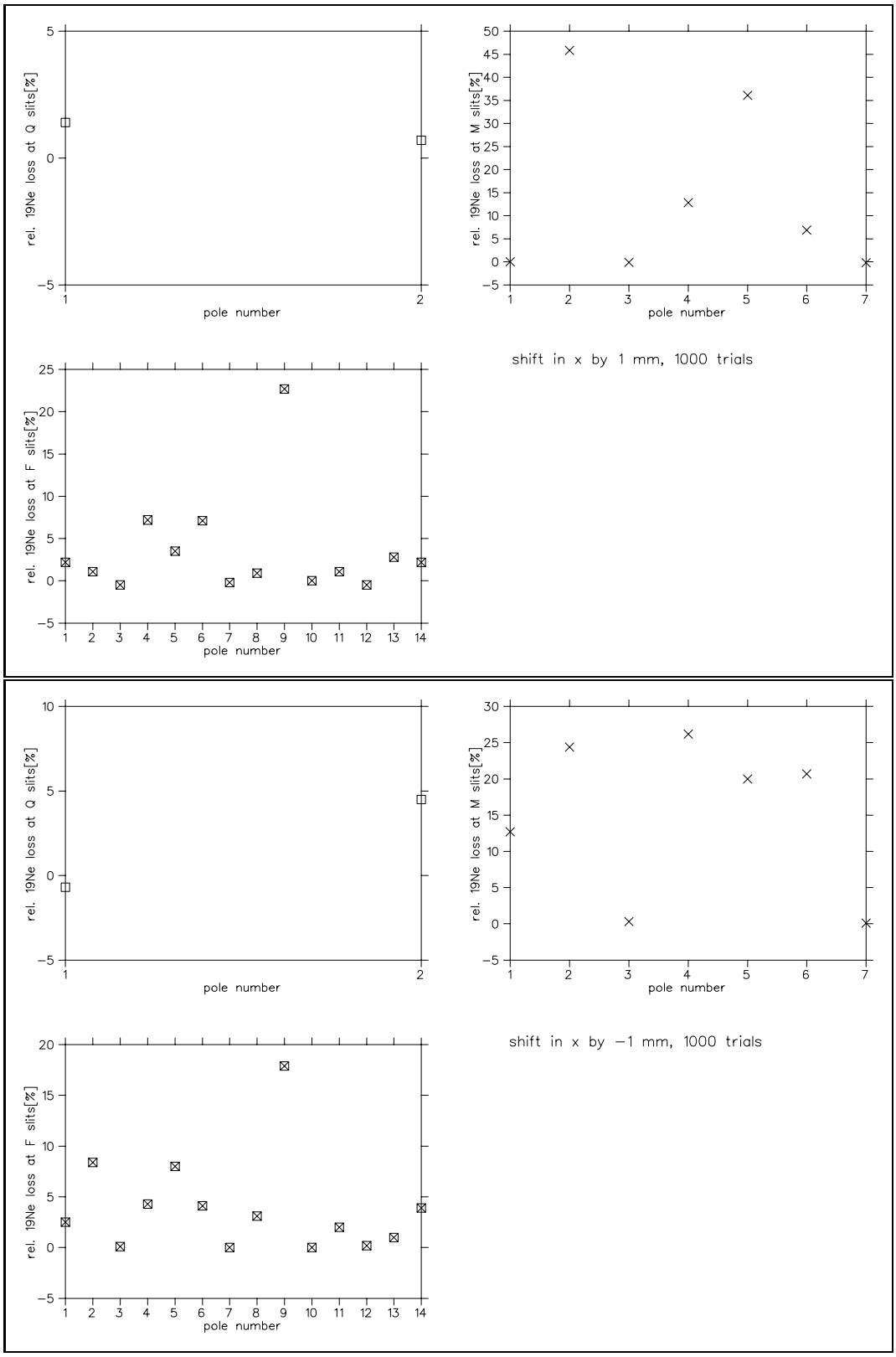

Figure 6.8: Incremental loss of ^{19}Ne at Q, M and F slits for independent horizontal shifts of quads and sextupoles of 1 and -1 mm.

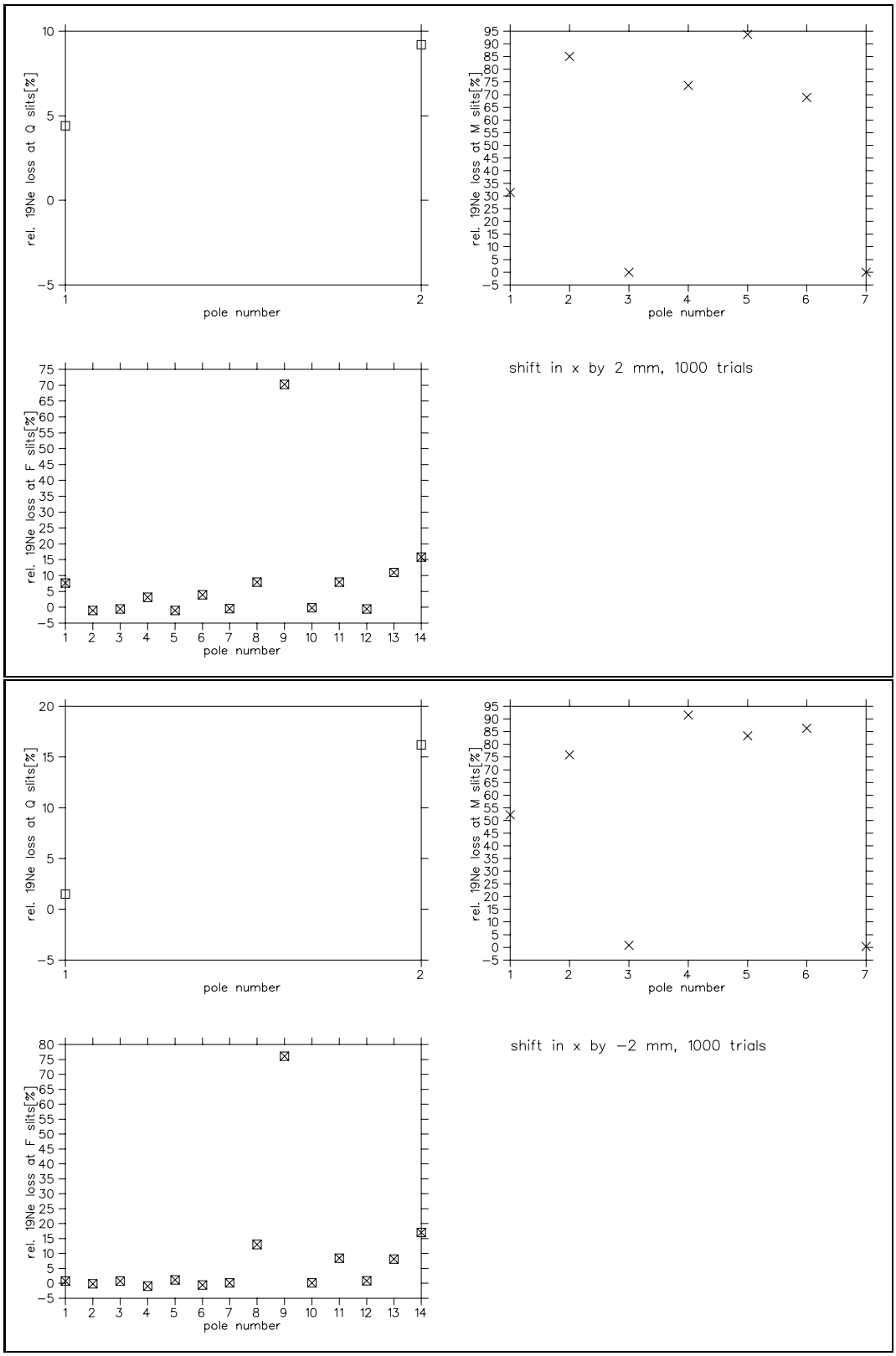

Figure 6.9: Incremental loss of ^{19}Ne at Q, M and F slits for independent horizontal shifts of quads and sextupoles of 2 and -2 mm.

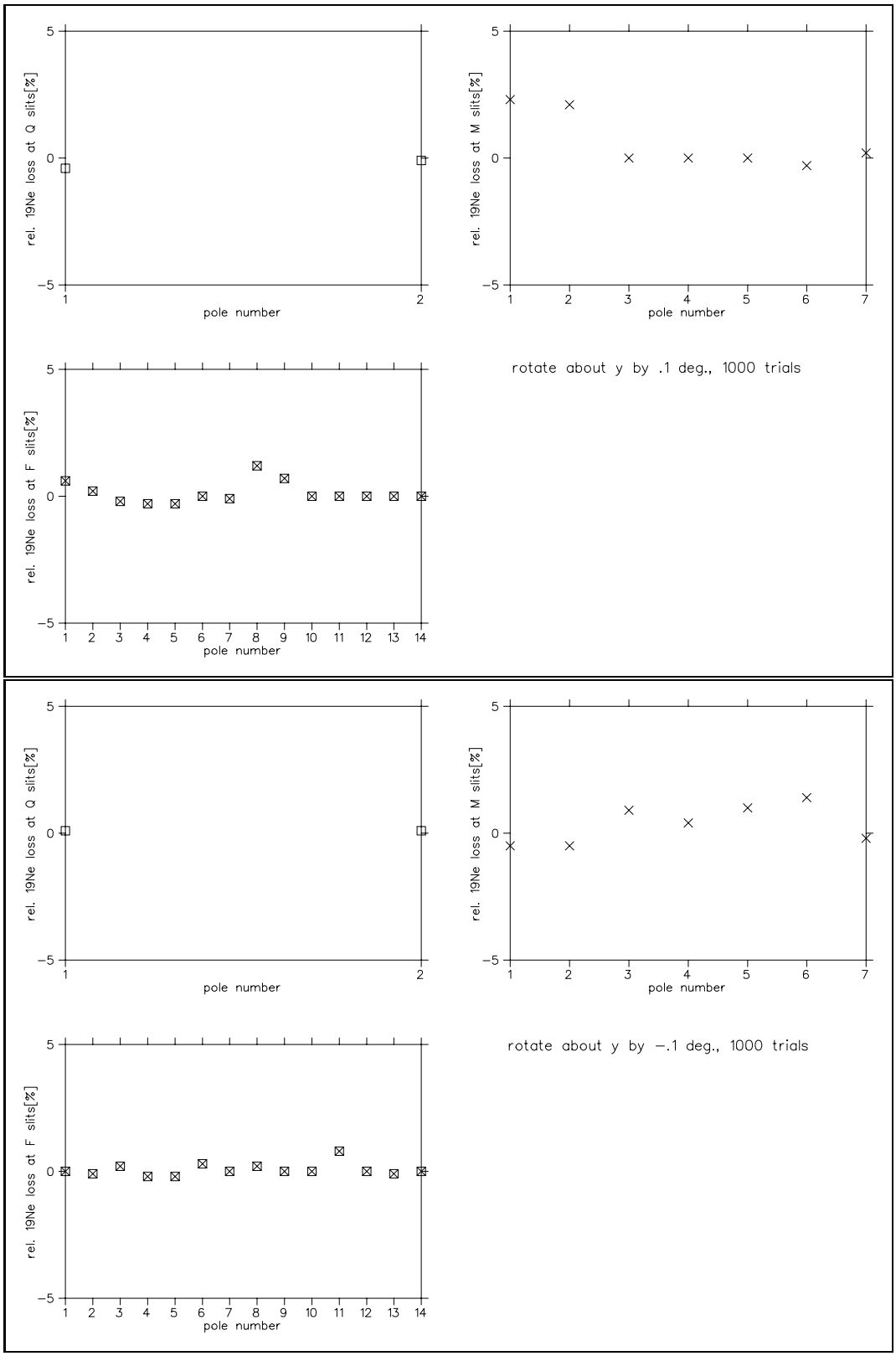

Figure 6.10: Incremental loss of ^{19}Ne at Q, M and F slits for independent rotations of quads and sextupoles about the vertical or y axis by .1 and -.1 degrees.

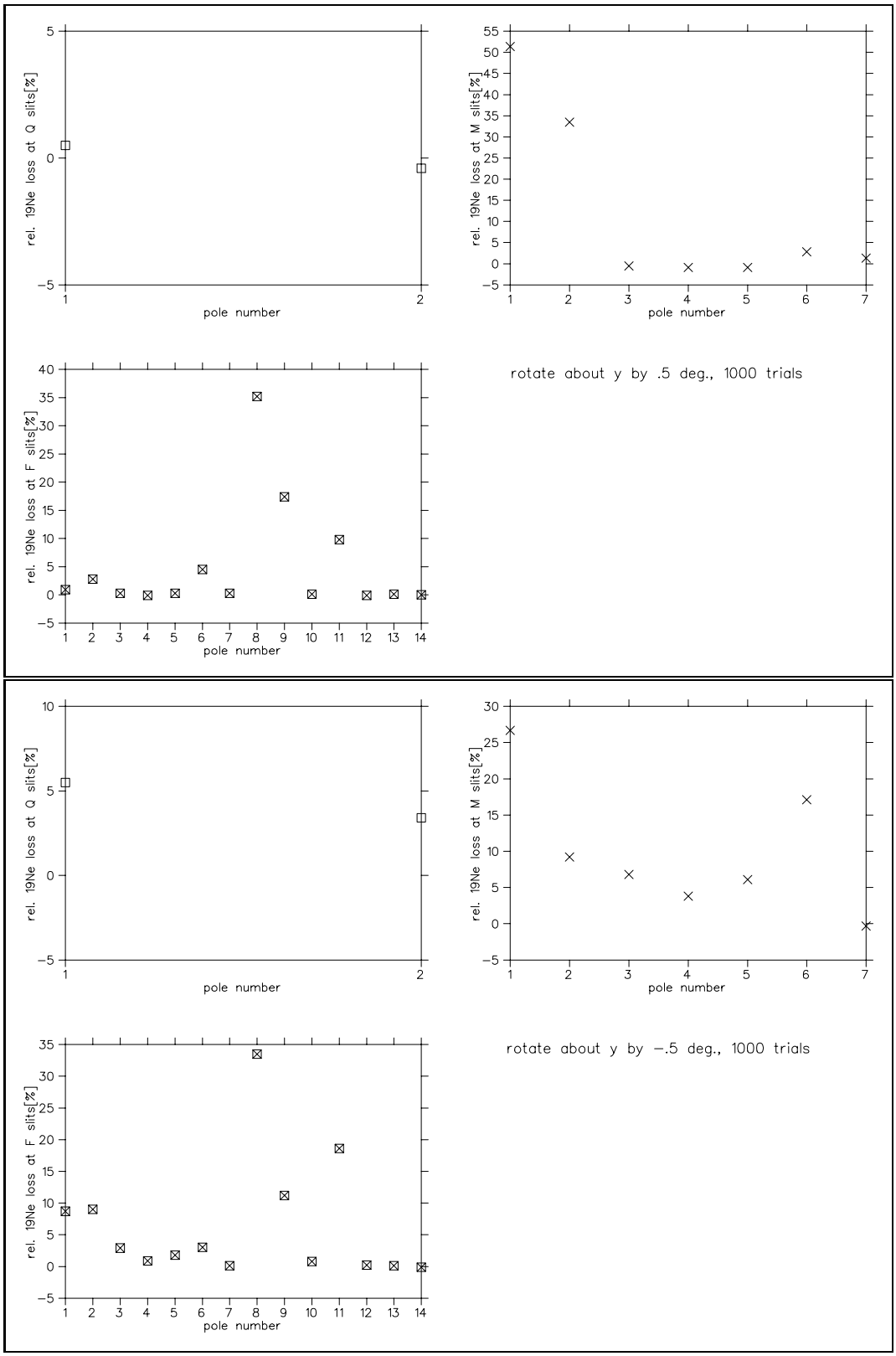

Figure 6.11: Incremental loss of ^{19}Ne at Q, M and F slits for independent rotations of quads and sextupoles about the vertical or y axis by .5 and -.5 degrees.

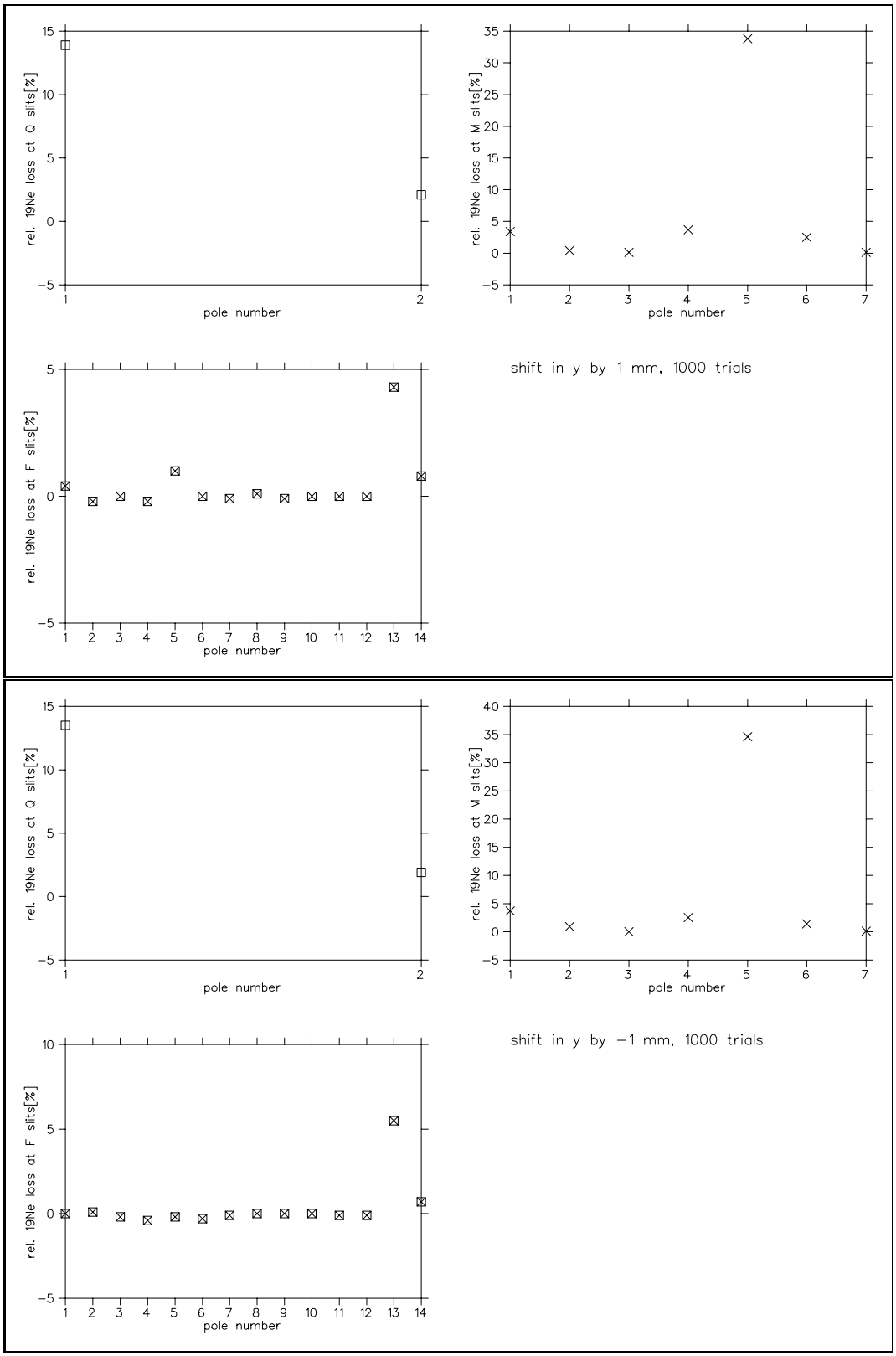

Figure 6.12: Incremental loss of ^{19}Ne at Q, M and F slits for independent vertical shifts of quads and sextupoles of 1 and -1 mm.

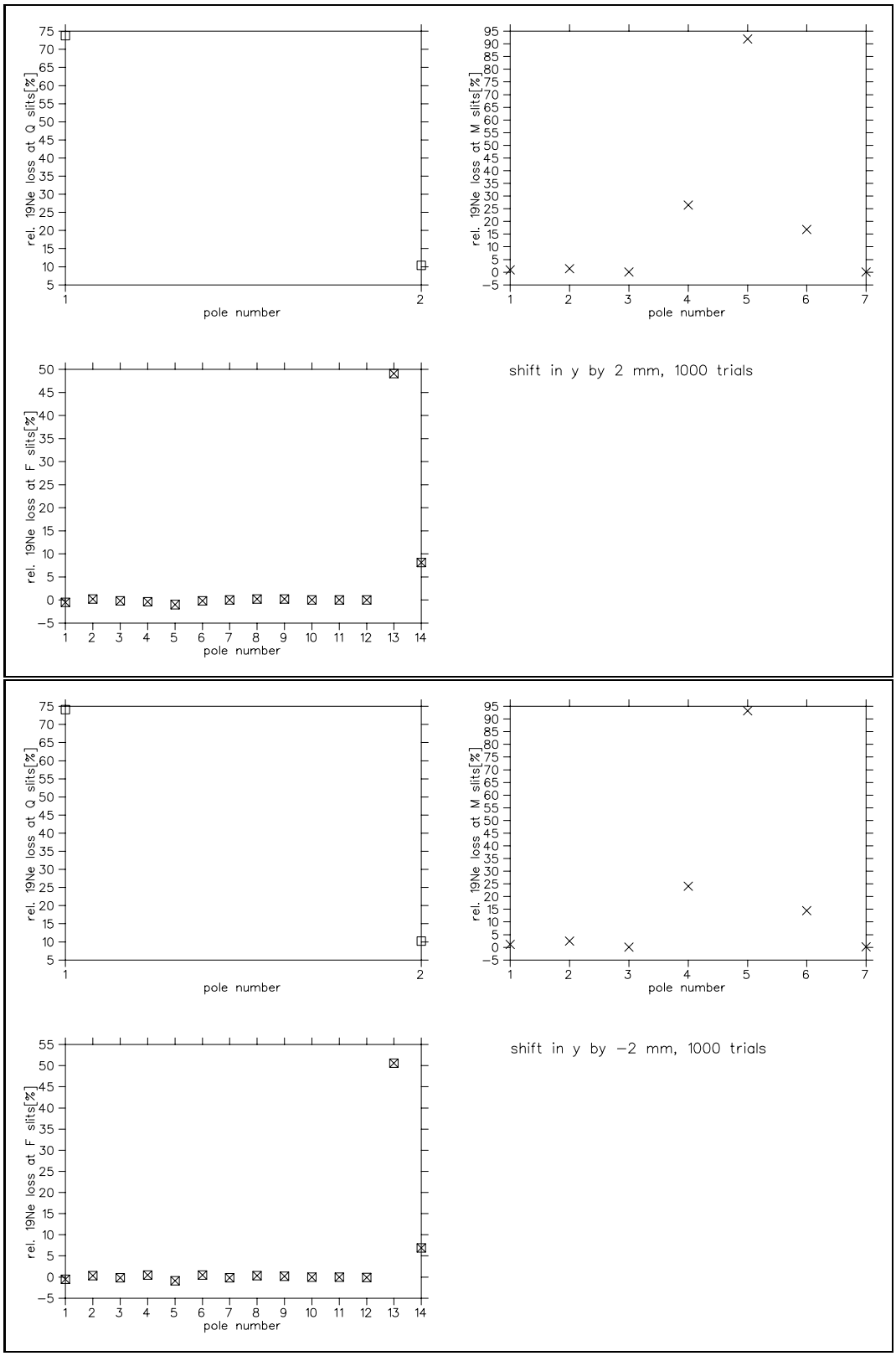

Figure 6.13: Incremental loss of ^{19}Ne at Q, M and F slits for independent vertical shifts of quads and sextupoles of 2 and -2 mm.

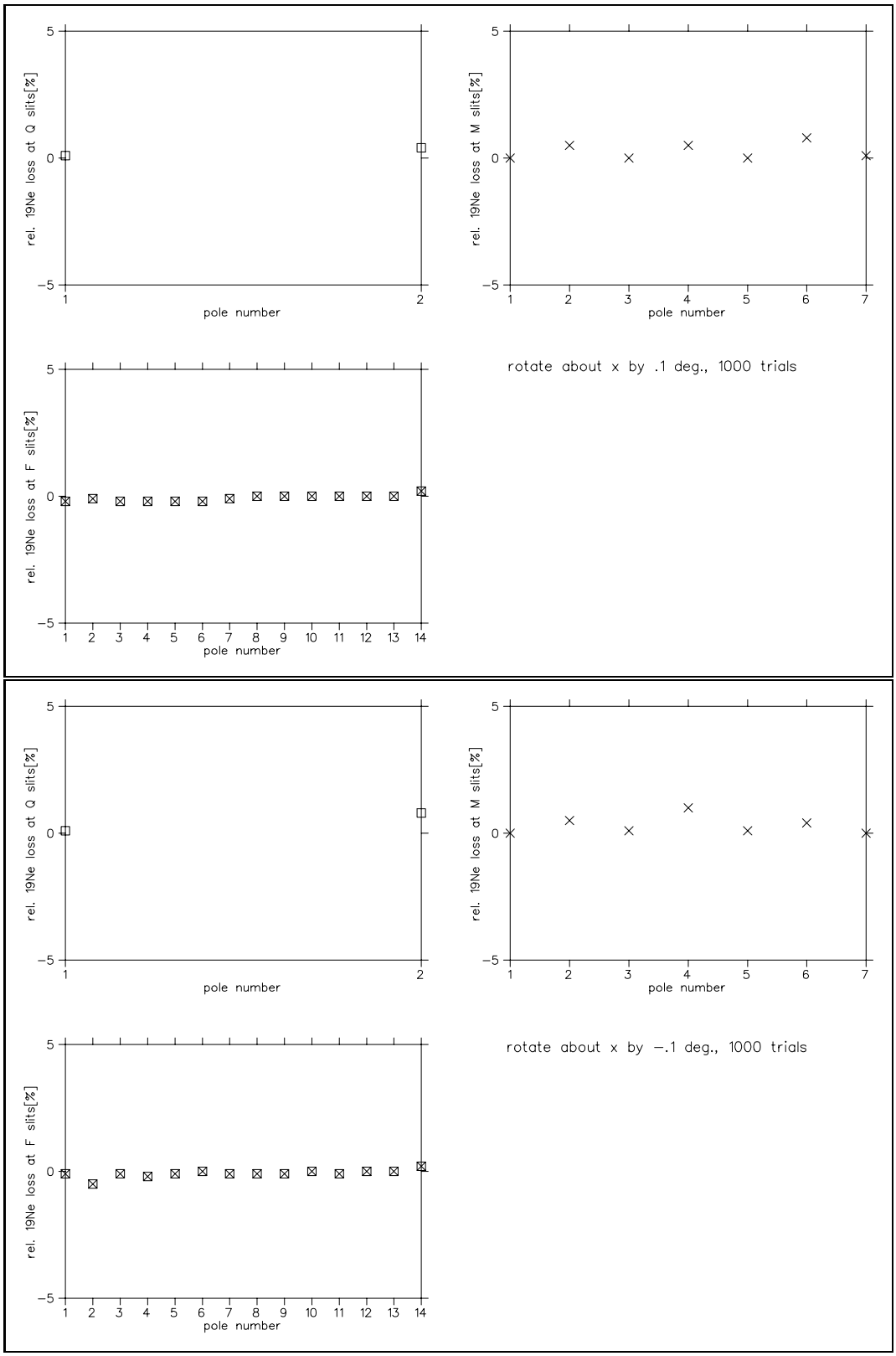

Figure 6.14: Incremental loss of ^{19}Ne at Q, M and F slits for independent rotations of quads and sextupoles about the horizontal or x axis by .1 and -.1 degrees.

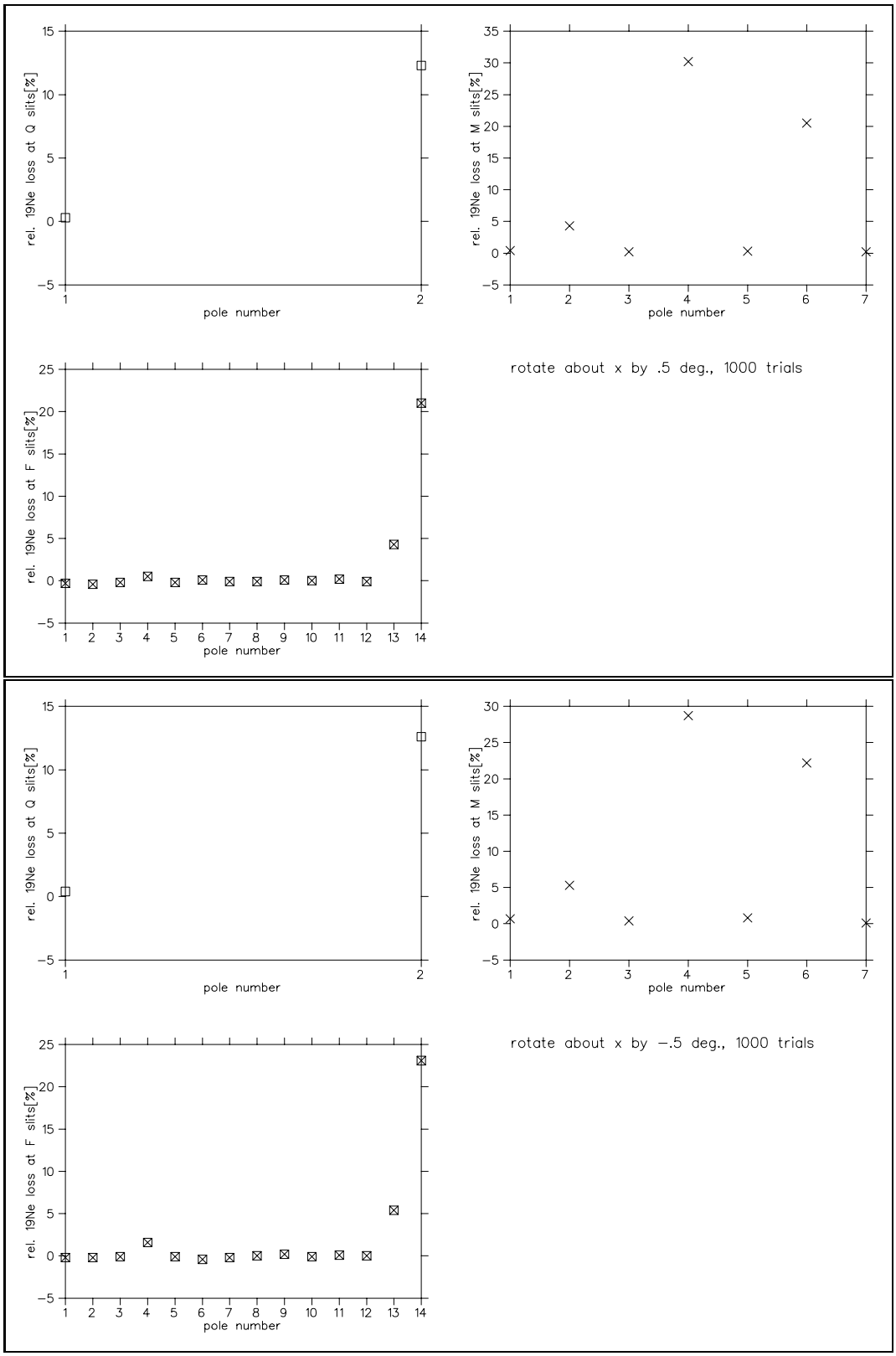

Figure 6.15: Incremental loss of ^{19}Ne at Q, M and F slits for independent rotations of quads and sextupoles about the horizontal or x axis by .5 and -.5 degrees.

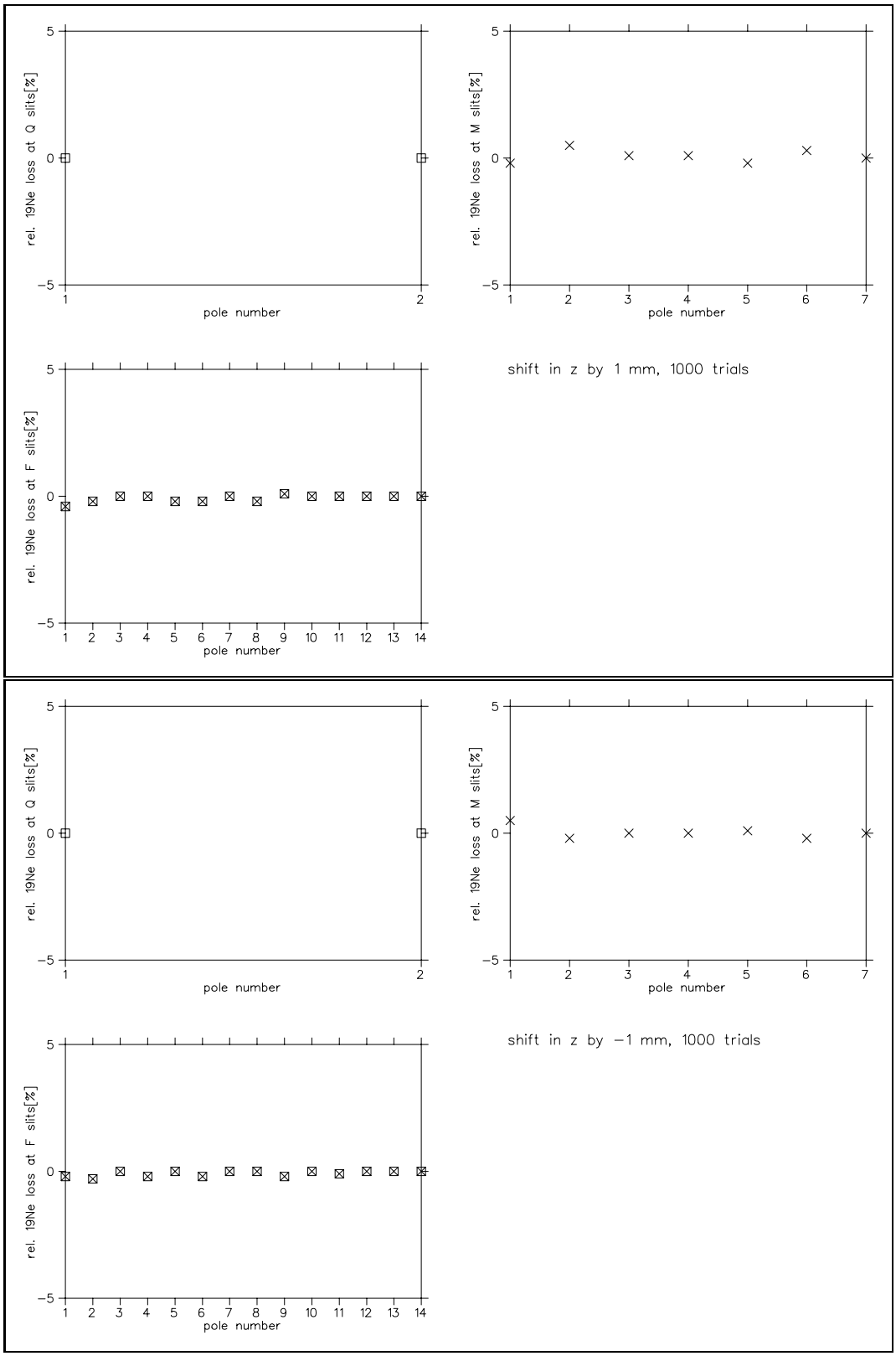

Figure 6.16: Incremental loss of ^{19}Ne at Q, M and F slits for independent longitudinal shifts of quads and sextupoles of 1 and -1 mm.

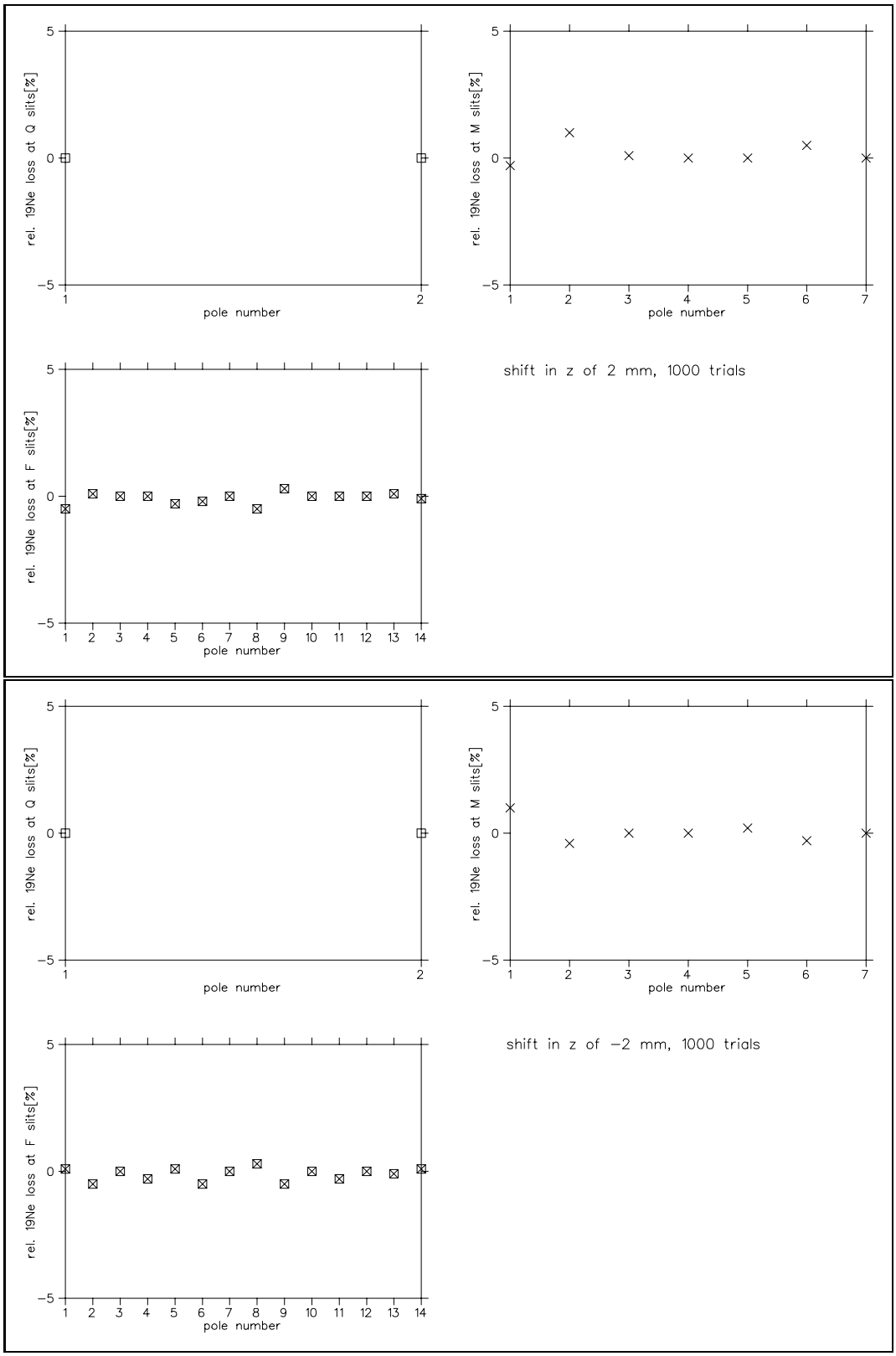

Figure 6.17: Incremental loss of ^{19}Ne at Q, M and F slits for independent longitudinal shifts of quads and sextupoles of 2 and -2 mm.

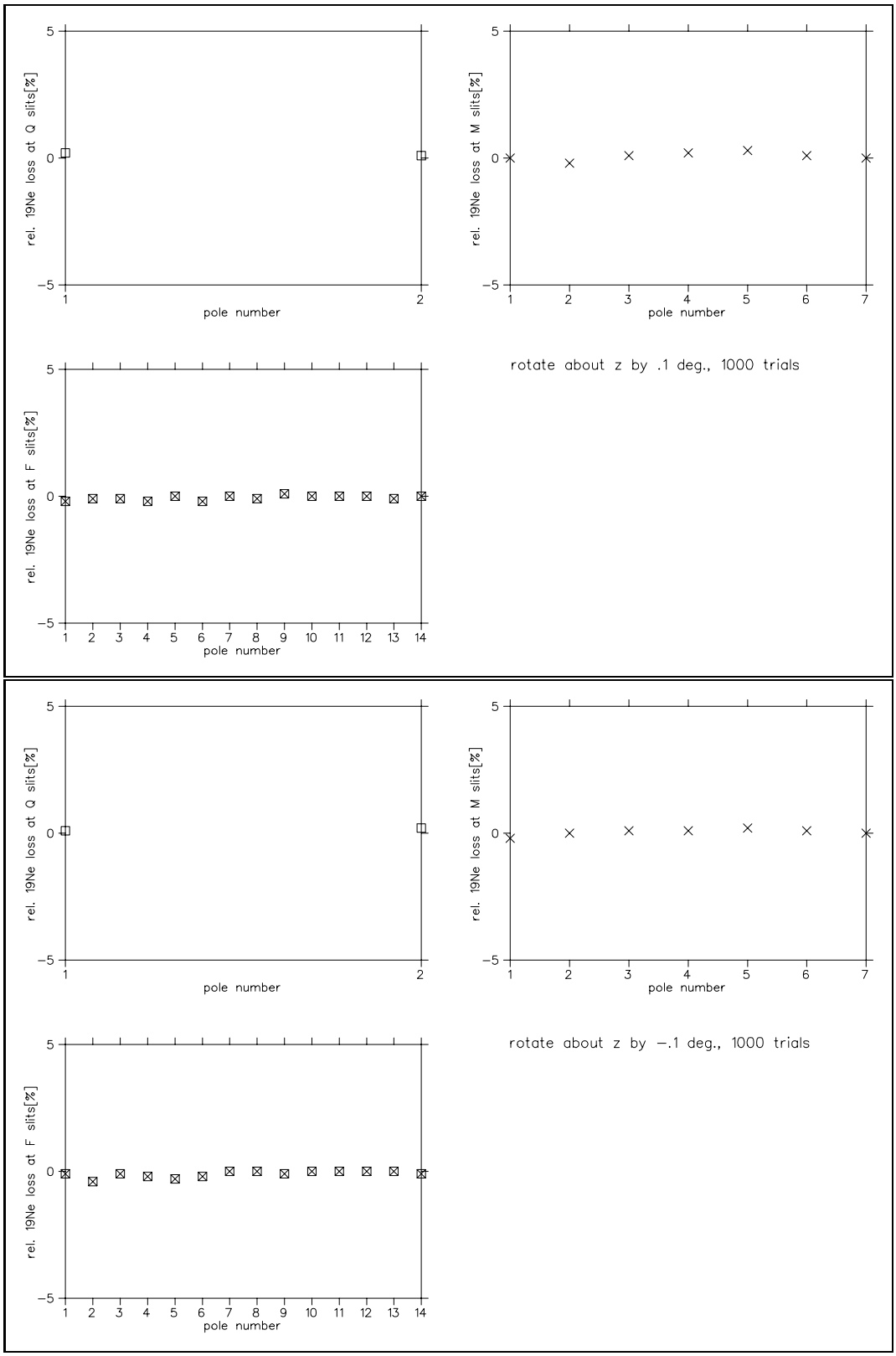

Figure 6.18: Incremental loss of ^{19}Ne at Q, M and F slits for independent rotations of quads and sextupoles about the longitudinal or z axis by .1 and -.1 degrees.

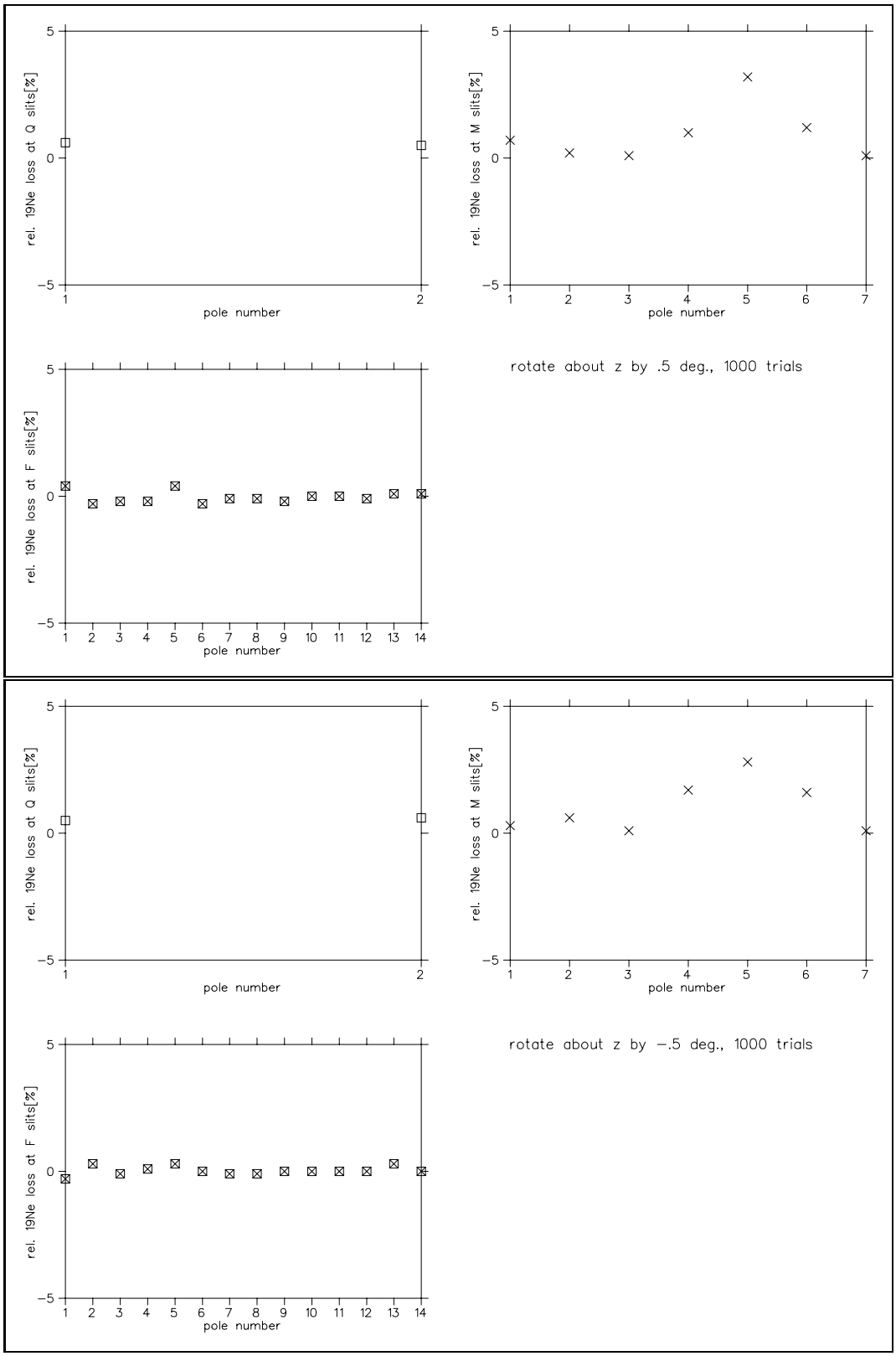

Figure 6.19: Incremental loss of ^{19}Ne at Q, M and F slits for independent rotations of quads and sextupoles about the longitudinal or z axis by .5 and -.5 degrees.

8. repeat for all steerers and dipole fields

Typically it takes 2 to 3 iterations to tune the central ray into the center of a monitor or slit location. Once a successful solution has been found using the central ray, a Monte Carlo simulation is run using several thousand $19_N e$ ions to compare the perturbed to the unperturbed case. This comparison focuses on the total transmission of $19_N e$ ions through the apparatus, and the emittance scans at several key locations.

6.4 Steerer calculations

Below is the RAYTRACE input file used to calculate the effect of a misorientation and correct it using the steerers and dipole field strengths. A shift or misorientation is achieved by placing shift-rotate commands before and after the lines for the component in question. The shift or misorientation after is in the opposite sense to that before (i.e. has the opposite sign). In order to reproduce a steerer action using a RAYTRACE magnetic dipole it is necessary to recover the optical axis after the steerer that existed before it. This is done using 2 consecutive SHRT commands following the dipole coding; for a horizontal(vertical) steerer the first shifting in the x(y) direction and the second rotating about the y(x) axis in the opposite sense to the steering.

'15O all ES ems 5 jan 98, 19Ne=1.8885 MeV, 15O=2.3921 MeV'
02000 500 1 2 0 0 0
1.8885, 0., 1., 19., 4.
DRIFT 1
0., 1.0,
COLD
1., 0., 0., 5., 5.
DRIFT 2
81.5, 2.0,
SHRT
-.0000182, 0., 0., 0., 0., 90.
DIPOLE ST0
2., 2., 2., 2., 3., 0.
0., 0., 10.16, 98005473., .00000022
.00001169, 0., .00001169
-0.0, -0., 0., -0.
16., -20., -20., 16.
0.2401, 5.5917, -5.0148, 10.5408, 0., 0.
0.2401, 5.5917, -5.0148, 10.5408, 0., 0.
0., 0., 0., 0., 0., 0.
-.0, 0.
0., 0., 0., 0., 0., 0., 0.
0., 0., 0., 0., 0., 0., 0.
SHRT
.00000204, 0., 0., 0., 0.00001169, 0.
SHRT
.0000182, 0., 0., 0., 0., -90.
DRIFT 3
5.0, 3.0,
SHRT
0., 0., 0., 0., 0., 0.
POLES Q1
3., 3., 3.
0., 0.1, 26., 5.
-0.0847924, .0, .0, 0., 0.
20., -20., -20., 20.
0.248, 6.37, -5.79, 5.915, 2.28, 0.
0.248, 6.37, -5.79, 5.915, 2.28, 0.
0.
SHRT
0., 0., 0., 0., 0., 0.
COLD
1., 0., 0., 5., 5.
DRIFT 4
0., 4.0,
COLD
1., 0., 0., 7.5, 7.5
DRIFT 5
24.5, 5.0,
SHRT
0., 0., 0., 0., 0., 0.
POLES Q2
3., 3., 3.
0., 0., 35., 7.5
.0775997, .0025, -.00, 0., 0.
20., -20., -20., 20.
0.248, 6.37, -5.79, 5.915, 2.28, 0.
0.248, 6.37, -5.79, 5.915, 2.28, 0.
0.
SHRT
0., 0., 0., 0., 0., 0.
COLD
1., 0., 0., 7.5, 7.5
DRIFT 6
0., 6.0,
COLD
0., 0., 0., 100., 5.
DRIFT 7
63., 7.0,
SHRT
-.2947, 0., 0., 0., 0., 0.
DIPOLE D1
2., 2., 2., 2., 3., 0.
0., 0., 10., 100., .21561204
50., 5.8349, 5.8349
-0.0, -0., 0., -0.
40., -43.635, -43.635, 40.
0.2401, 1.8639, -.5572, .3904, 0., 0.
0.2401, 1.8639, -.5572, .3904, 0., 0.
0., 0., 0., 0., 0., 0.
-.0, 0.
0., 0., 0., 0., 0., 0., 0.
0., 0., 0., 0., 0., 0., 0.
SHRT
.2947, 0., 0., 0., 0., 0.

```
COLD
0., 0., 0., 100., 5.
DRIFT 8
0., 8.0,
DRIFT 9
30.79, 9.0,
COLD Q slits
0., 0., 0., 1.1, 1.3
DRIFT 10
0., 10.0,
COLD
1., 0., 0., 7.5, 7.5
DRIFT 11
21.5, 11.0,
SHRT
-0.014, 0., 0., 0., 0., 0.
DIPOLE ST1
2., 2., 2., 2., 3., 0.
0., 0., 15.875, 98005473., .00000022
.00002163, 0., .00002163
-0.0, -0., 0., -0.
16., -20., -20., 16.
0.2401, 5.5917, -5.0148, 10.5408, 0., 0.
0.2401, 5.5917, -5.0148, 10.5408, 0., 0.
0., 0., 0., 0., 0., 0.
-.0, 0.
0., 0., 0., 0., 0., 0., 0.
0., 0., 0., 0., 0., 0., 0.
SHRT
.00000698, 0., 0., 0., 0.00002163, 0.
SHRT
0.014, 0., 0., 0., 0., 0.
DRIFT 12
0., 12.0,
DRIFT 13
17.0, 13.0,
SHRT
0., 0., 0., 0., 0., 0.
POLES S1
3., 3., 3.
0., .0, 10., 7.5
0., .028, 0., 0., 0.
20., -20., -20., 20.
0., 0., 0., 0., 0., 0.
0., 0., 0., 0., 0., 0.
0.
SHRT
0., 0., 0., 0., 0., 0.
COLD
1., 0., 0., 7.5, 7.5
DRIFT 14
0., 14.0,
COLD
1., 0., 0., 7.5, 7.5
DRIFT 15
20., 15.0,
SHRT
0., 0., 0., 0., 0., 0.
POLES Q3
3., 3., 3.
0., 0., 35., 7.5
.07085947, 0., 0., 0., 0.
20., -20., -20., 20.
0.248, 6.37, -5.79, 5.915, 2.28, 0.
0.248, 6.37, -5.79, 5.915, 2.28, 0.
0.
SHRT
0., 0., 0., 0., 0., 0.
COLD
1., 0., 0., 7.5, 7.5
DRIFT 16
0., 16.0,
COLD
1., 0., 0., 7.5, 7.5
DRIFT 17
20., 17.0,
SHRT
0., 0., 0., 0., 0., 0.
POLES Q4
3., 3., 3.
0., 0., 35., 7.5
-.09349109, 0., 0., 0., 0.
20., -20., -20., 20.
0.248, 6.37, -5.79, 5.915, 2.28, 0.
0.248, 6.37, -5.79, 5.915, 2.28, 0.
0.
```

```
SHRT
0., 0., 0., 0., 0., 0.
COLD
1., 0., 0., 7.5, 7.5
DRIFT 18
0., 18.0,
DRIFT 19
20., 19.0,
SHRT
0., 0., 0., 0., 0., 0.
POLES Q5
3., 3., 3.
0., 0., 35., 7.5
0.05150688, 0., 0., 0., 0.
20., -20., -20., 20.
0.248, 6.37, -5.79, 5.915, 2.28, 0.
0.248, 6.37, -5.79, 5.915, 2.28, 0.
0.
SHRT
0., 0., 0., 0., 0., 0.
COLD
1., 0., 0., 7.5, 7.5
DRIFT 20
0., 20.0,
COLD
1., 0., 0., 7.5, 7.5
DRIFT 21
20., 21.0,
SHRT
0., 0., 0., 0., 0., 0.
POLES S2
3., 3., 3.
0., 0., 10., 7.5
0., .0045, 0., 0., 0.
20., -20., -20., 20.
0., 0., 0., 0., 0., 0.
0., 0., 0., 0., 0., 0.
0.
SHRT
0., 0., 0., 0., 0., 0.
COLD
1., 0., 0., 7.5, 7.5
DRIFT 22
0., 22.0,
DRIFT 23
35., 23.0,
COLD mon1
0., 0., 0., 5., 5.
DRIFT 24
50., 24.0,
SHRT
-.1373, 0., 0., 0., 0., 0.
EDIP ES1
1., 1., 1., .6
0., 0., 10., 200., 4.721
20.
0., 0., 0., 0
20., -30., -30., 20.
.10419, 4.1163, -.49773, 1.3688, -.49696, -.07316
.10419, 4.1163, -.49773, 1.3688, -.49696, -.07316
SHRT
.1373, 0., 0., 0., 0., 0.
COLD
0., 0., 0., 5., 5.
DRIFT 25
0., 25.0,
DRIFT 26
105., 26.0,
COLD M slits
0., 0., 0., .37, 1.2
DRIFT 27
0., 27.0,
COLD
1., 0., 0., 7.5, 7.5
DRIFT 28
22., 28.0,
SHRT
-0.014, 0., 0., 0., 0., 0.
DIPOLE ST2
2., 2., 2., 2., 3., 0.
0., 0., 15.875, 98005473., .00000022
.00002163, 0., .00002163
-0.0, -0., 0., -0.
16., -20., -20., 16.
0.2401, 5.5917, -5.0148, 10.5408, 0., 0.
0.2401, 5.5917, -5.0148, 10.5408, 0., 0.
```

0., 0., 0., 0., 0., 0.
-.0, 0.
0., 0., 0., 0., 0., 0., 0.
0., 0., 0., 0., 0., 0., 0.
SHRT
.00000698, 0., 0., 0., 0.00002163, 0.
SHRT
0.014, 0., 0., 0., 0., 0.
DRIFT 29
0., 29.0,
DRIFT 30
21., 30.0,
SHRT
0., 0., 0., 0., 0.
POLES Q6
3., 3., 3.
0., 0., 26., 5.
-.04388486, 0., 0., 0., 0.
20., -20., -20., 20.
0.248, 6.37, -5.79, 5.915, 2.28, 0.
0.248, 6.37, -5.79, 5.915, 2.28, 0.
0.
SHRT
0., 0., 0., 0., 0., 0.
COLD
1., 0., 0., 7.5, 7.5
DRIFT 31
0., 31.0,
COLD
1., 0., 0., 7.5, 7.5
DRIFT 32
24.5, 32.0,
SHRT
0., 0., 0., 0., 0., 0.
POLES Q7
3., 3., 3.
0., 0., 35., 7.5
.06519025, 0., 0., 0., 0.
20., -20., -20., 20.
0.248, 6.37, -5.79, 5.915, 2.28, 0.
0.248, 6.37, -5.79, 5.915, 2.28, 0.
0.
SHRT
0., 0., 0., 0., 0., 0.
COLD
1., 0., 0., 7.5, 7.5
DRIFT 33
20., 33.0,
SHRT
0., 0., 0., 0., 0., 0.
POLES S3
3., 3., 3.
0., 0., 10., 7.5
0., .003543, -.001936, 0., 0.
20., -20., -20., 20.
0., 0., 0., 0., 0., 0.
0., 0., 0., 0., 0., 0.
0.
SHRT
0., 0., 0., 0., 0., 0.
COLD
1., 0., 0., 7.5, 7.5
DRIFT 34
0., 34.0,
COLD
0., 0., 0., 40., 3.5
DRIFT 35 mon2
13., 35.0,
DRIFT 36
37., 36.0,
SHRT
-.37814, 0., 0., 0., 0., 0.
DIPOLE D2
1., 1., 1., 1., 3., 0.
0., 0., 12., 81.3, .26520546
75., 29., 29.
-0.00, -0., 0., -0.
39.4345, -36.7655, -36.7655, 39.4345
.1858, 3.62012, -.584425, -.222664, .056817, .006777
.1858, 3.62012, -.584425, -.222664, .056817, .006777
0., 0., 0., 0., 0., 0.
0., 0.
0., 0., 0., 0., 0., 0., 0.
0., 0., 0., 0., 0., 0., 0.
SHRT
.37814, 0., 0., 0., 0., 0.

```
COLD
0., 0., 0., 40., 3.5
DRIFT 37
0., 37.0,
DRIFT 38 mon3
56.076, 38.0,
DRIFT 39
6.5, 39.0,
SHRT
-0.014, 0., 0., 0., 0., 0.
DIPOLE ST3
2., 2., 2., 2., 3., 0.
0., 0., 15.875, 98005473., .00000022
.00002163, 0., .00002163
-0.0, -0., 0., -0.
16., -20., -20., 16.
0.2401, 5.5917, -5.0148, 10.5408, 0., 0.
0.2401, 5.5917, -5.0148, 10.5408, 0., 0.
0., 0., 0., 0., 0., 0.
-.0, 0.
0., 0., 0., 0., 0., 0., 0.
0., 0., 0., 0., 0., 0., 0.
SHRT
.00000698, 0., 0., 0., 0.00002163, 0.
SHRT
0.014, 0., 0., 0., 0., 0.
DRIFT 40
17.724, 40.0,
COLD
1., 0., 0., 7.5, 7.5
SHRT
0., 0., 0., 0., 0., 0.
POLES Q8
3., 3., 3.
0., 0., 35., 7.5
0.04883185, 0., 0., 0., 0.
20., -20., -20., 20.
0.248, 6.37, -5.79, 5.915, 2.28, 0.
0.248, 6.37, -5.79, 5.915, 2.28, 0.
0.
SHRT
0., 0., 0., 0., 0., 0.
COLD
1., 0., 0., 7.5, 7.5
DRIFT 41
0., 41.0,
COLD
1., 0., 0., 7.5, 7.5
DRIFT 42
20., 42.0,
SHRT
0., 0., 0., 0., 0., 0.
POLES S4
3., 3., 3.
0., 0., 10., 7.5
0., .02898, 0., 0., 0.
20., -20., -20., 20.
0., 0., 0., 0., 0., 0.
0., 0., 0., 0., 0., 0.
0.
SHRT
0., 0., 0., 0., 0., 0.
COLD
1., 0., 0., 7.5, 7.5
DRIFT 43
0., 43.0,
COLD
0., 0., 0., 5., 15.
DRIFT 44 mon4
40., 44.0,
DRIFT 45
50., 45.0,
SHRT
-.2537, 0., 0., 0., 0., 0.
EDIP ES2
1., 1., 1., .6
0., 0., 10., 250., 3.77179869
35.
0., 0., 50., 0.
20., -30., -30., 20.
.10419, 4.1163, -.4977, 1.3688, -.497, -.07316
.10419, 4.1163, -.4977, 1.3688, -.497, -.07316
SHRT
.2537, 0., 0., 0., 0., 0.
COLD
0., 0., 0., 5., 15.
```

```
DRIFT 46
0., 46.0,
COLD
1., 0., 0., 7.5, 7.5
DRIFT 47 mon 5
50., 47.0,
DRIFT 48
6.5, 48.0,
SHRT
-0.014, 0., 0., 0., 0., 0.
DIPOLE ST4
2., 2., 2., 2., 3., 0.
0., 0., 15.875, 98005473., .00000022
.00002163, 0., .00002163
-0.0, -0., 0., -0.
16., -20., -20., 16.
0.2401, 5.5917, -5.0148, 10.5408, 0., 0.
0.2401, 5.5917, -5.0148, 10.5408, 0., 0.
0., 0., 0., 0., 0., 0.
-.0, 0.
0., 0., 0., 0., 0., 0., 0.
0., 0., 0., 0., 0., 0., 0.
SHRT
.00000698, 0., 0., 0., 0.00002163, 0.
SHRT
0.014, 0., 0., 0., 0., 0.
DRIFT 49
6.5, 49.0,
SHRT
0., 0., 0., 0., 0., 0.
POLES Q9
3., 3., 3.
0., 0., 35., 7.5
-.0561972, 0., 0., 0., 0.
20., -20., -20., 20.
0.248, 6.37, -5.79, 5.915, 2.28, 0.
0.248, 6.37, -5.79, 5.915, 2.28, 0.
0.
SHRT
0., 0., 0., 0., 0., 0.
COLD
1., 0., 0., 7.5, 7.5
DRIFT 50
0., 50.0,
COLD
1., 0., 0., 7.5, 7.5
DRIFT 51
20., 51.0,
SHRT
0., 0., 0., 0., 0., 0.
POLES Q10
3., 3., 3.
0., 0., 35., 7.5
.05581396, 0., 0., 0., 0.
20., -20., -20., 20.
0.248, 6.37, -5.79, 5.915, 2.28, 0.
0.248, 6.37, -5.79, 5.915, 2.28, 0.
0.
SHRT
0., 0., 0., 0., 0., 0.
COLD
1., 0., 0., 7.5, 7.5
DRIFT 52
0., 52.0,
DRIFT 53
160.9193, 53.0,
COLD
0., -.15, 0., .65, .8
DRIFT 54
0., -54.0,
SENTINEL
```

Bibliography

[1] A.J.H. Boerboom, Int. Jour. Mass Spec. and Ion Physics **45**22(1976)259.

[2] H-D. Betz,*Rev. Mod. Phys.*, 44(3) (1972)465

[3] J. R. Macdonald et al,*Phys. Rev. A*, 4(5) (1971)1965

[4] Wu et al, *At. Data and Nucl. data Tables*, 40 (1988)57

[5] K. Shima et al, *At. Data and Nucl. data Tables*, 51 (1992)173

[6] R. C. Dehmel et al, *Atomic Data*, 5 (1971)231

[7] A. S. Schlachter et al, *Phys. Rev. A*, 27(11) (1983)3372

[8] G.D.Alton et al,*Phys. Rev. A*, 23 (1981)1073

[9] A. Gavron,*Nucl. Instr. and Meth. A*, **336** (1993)269

[10] A.J.H. Boerboom, *Int. Jour. Mass Spec. and Ion Physics*, **45**22(1976)259.

[11] L.I.Schiff,*Quantum Mechanics*, McGraw Hill, New York, 1955, p. 170

Chapter 7

Appendix

This is the most recent RAYTRACE input file, res2000.dat, that incorporates the Enge fringing fields calculated by fitting to the field maps of Doug Evans and the Opera3D calculations of Bruce Milton for ED_1 and ED_2.

```
'15O 28 Sept 00, 19Ne=1.8885 MeV,
15O=2.3921 MeV; use M13/15 sext'
09900 500 1 2 0 0 0
1.8885, 0., 1., 19., 4.
DRIFT 1
0., 1.0,
COLD
1., 0., 0., .4, .4
DRIFT 2
5., 2.0,
COLD
1., 0., 0., 1.8, 1.8
DRIFT 3
70., 3.0,
COLD
1., 0., 0., 5., 5.
DRIFT 4
6.5, 4.0,
SHRT
-.0000182, 0., 0., 0., 0., 90.
DIPOLE ST0
2., 2., 2., 2., 3., 0.
0., 0., 10.16, 98005473., .00000022
.00001169, 0., .00001169
-0.0, -0., 0., -0.
16., -20., -20., 16.
0.2401, 5.5917, -5.0148, 10.5408, 0., 0.
0.2401, 5.5917, -5.0148, 10.5408, 0., 0.
0., 0., 0., 0., 0., 0.
-.0, 0.
0., 0., 0., 0., 0., 0., 0.
0., 0., 0., 0., 0., 0., 0.
SHRT
.00000204, 0., 0., 0., 0.00001169, 0.
SHRT
.0000182, 0., 0., 0., 0., -90.
COLD
1., 0., 0., 5., 5.
DRIFT 5
5.385, 5.0,
SHRT
0., 0., 0., 0., 0., 0.
POLES Q1
3., 3., 3.
0., 0., 25.23, 5.3975
-0.09432691, .0, .0, 0., 0.
18.89, -13.494, -13.494, 18.89
.295, 6.30221, -3.51059, .29528, 1.19866, -.423408
.295, 6.30221, -3.51059, .29528, 1.19866, -.423408
0.
SHRT
-0., 0., 0., 0., 0., 0.
COLD
1., 0., 0., 5., 5.
DRIFT 6
0., 6.0,
COLD
1., 0., 0., 7.5, 7.5
DRIFT 7
25.6925, 7.0,
SHRT
0., 0., 0., 0., 0., 0.
POLES Q2
3., 3., 3.
0., 0., 33.385, 7.9375
.08637239, .0045675, -.00, 0., -.0
23.813, -19.844, -19.844,23.813
0.22, 5.367112, -1.99912, .911917, -.663814,
.348883
0.22, 5.367112, -1.99912, .911917, -.663814,
.348883
0.
SHRT
-0., 0., 0., 0., -.0, 0.
COLD
1., 0., 0., 7.5, 7.5
DRIFT 8
0., 8.0,
COLD 1st BCM bellows
1., 0., 0., 7.409, 7.409
DRIFT 9
26.8, 9.0,
COLD 2nd BCM bellows
1., 0., 0., 7.409, 7.409
DRIFT 10
26., 10.0,
COLD
0., 0., 0., 100., 4.
DRIFT
11.0075
SHRT
-.19107, 0., 0., 0., 0., 0.
```

DIPOLE D1
2., 2., 2., 2., 3., 0.
0., 0., 10., 100., .21561204
50., 5.8, 5.8
-0.0, -0., 0., -0.
30., -22., -22., 30.
.2877, 3.52101, -1.02159, -.049652, .133009,
-.0193801
.2877, 3.52101, -1.02159, -.049652, .133009,
-.0193801
0., 0., 0., 0., 0., 0.
-.0, 0.
0., 0., 0., 0., 0., 0., 0.
0., 0., 0., 0., 0., 0., 0.
SHRT
.19107, 0., 0., 0., 0., 0.
COLD
0., 0., 0., 100., 4.
DRIFT
0.
DRIFT 11
30.79, 11.0,
COLD Q slits
0., 0., 0., 1.16, 1.1
DRIFT 12
0., 12.0,
COLD
1., 0., 0., 7.5, 7.5
DRIFT 13
27.2, 13.0,
SHRT
-0.014, 0., 0., 0., 0., 0.
DIPOLE ST1
2., 2., 2., 2., 3., 0.
0., 0., 15.875, 67809192., .00000022
.00002163, 0., .00002163
-0.0, -0., 0., -0.
16., -20., -20., 16.
0.2401, 5.5917, -5.0148, 10.5408, 0., 0.
0.2401, 5.5917, -5.0148, 10.5408, 0., 0.
0., 0., 0., 0., 0., 0.
-.0, 0.
0., 0., 0., 0., 0., 0., 0.
0., 0., 0., 0., 0., 0., 0.
SHRT
.00000698, 0., 0., 0., 0.00002163, 0.
SHRT
0.014, 0., 0., 0., 0., 0.
DRIFT 14
0., 14.0,
DRIFT 15
18.62, 15.0,
SHRT
0., 0., 0., 0., 0., 0.
POLES S1
3., 3., 3.
0., .0, 18.75, 7.95
0., .01831480, 0., 0., 0.
20., -20., -20., 20.
0., 0., 0., 0., 0., 0.
0., 0., 0., 0., 0., 0.
0.
SHRT
0., 0., 0., 0., 0., 0.
COLD
1., 0., 0., 7.5, 7.5
DRIFT 16
0., 16.0,
COLD
1., 0., 0., 7.5, 7.5
DRIFT 17
16.14, 17.0,
SHRT
0., 0., 0., 0., 0., 0.
POLES Q3
3., 3., 3.
0., 0., 33.38, 7.9375
.07875767, 0., 0., 0., 0.
23.813, -19.844, -19.844,23.813
0.225, 6.22466, -2.38148, .2341, -.72032, .72371
0.225, 6.22466, -2.38148, .2341, -.72032, .72371
0.
SHRT
0., 0., 0., 0., 0., 0.
COLD
1., 0., 0., 7.5, 7.5
DRIFT 18
0., 18.0,
COLD
1., 0., 0., 7.5, 7.5
DRIFT 19
21.62, 19.0,
SHRT
0., 0., 0., 0., 0., 0.
POLES Q4
3., 3., 3.
0., 0., 33.38, 7.9375
-.10400018, .00, 0., 0., 0.
23.813, -19.844, -19.844,23.813
0.225, 6.22466, -2.38148, .2341, -.72032, .72371
0.225, 6.22466, -2.38148, .2341, -.72032, .72371
0.

```
SHRT
0., 0., 0., 0., 0., 0.
COLD
1., 0., 0., 7.5, 7.5
DRIFT 20
0., 20.0,
DRIFT 21
21.62, 21.0,
SHRT
0., 0., 0., 0., 0., 0.
POLES Q5
3., 3., 3.
0., 0., 33.38, 7.9375
.05728922, .00, 0., 0., 0.
23.813, -19.844, -19.844,23.813
0.225, 6.22466, -2.38148, .2341, -.72032, .72371
0.225, 6.22466, -2.38148, .2341, -.72032, .72371
0.
SHRT
0., 0., 0., 0., 0., 0.
COLD
1., 0., 0., 7.5, 7.5
DRIFT 22
0., 22.0,
COLD
1., 0., 0., 7.5, 7.5
DRIFT 23
16.14, 23.0,
SHRT
0., 0., 0., 0., 0., 0.
POLES S2
3., 3., 3.
0., 0., 19.41, 7.95
0., .00385606, 0., 0., 0.
20., -20., -20., 20.
0., 0., 0., 0., 0., 0.
0., 0., 0., 0., 0., 0.
0.
SHRT
0., 0., 0., 0., 0., 0.
COLD
1., 0., 0., 7.5, 7.5
DRIFT 24
0., 24.0,
COLD 1st BCM bellows
1., 0., 0., 7.409, 7.409
DRIFT 25
15.23, 25.0,
COLD 2nd BCM bellows
1., 0., 0., 7.409, 7.409
DRIFT 26
26., 26.0,
DRIFT
39.69
SHRT
-.0657, 0., 0., 0., 0., 0.
EDIP ED1
1., 1., 1., .6
0., 0., 10., 200., 4.721
20.
0., 0., 0., 0
15.1658, -14.6504, -14.6504, 15.1658
.07901, 3.90918, -.65329, 1.91401, .22838, -.80791
.07901, 3.90918, -.65329, 1.91401, .22838, -.80791
SHRT
.0657, 0., 0., 0., 0., 0.
COLD
0., 0., 0., 5., 5.
DRIFT 27
0., 27.0,
DRIFT 28
105., 28.0,
COLD M slits
0., .0, .0, .24, 1.2
DRIFT 29
0., 29.0,
COLD
1., 0., 0., 7.5, 7.5
DRIFT 30
27.7, 30.0,
SHRT
-0.014, 0., 0., 0., 0., 0.
DIPOLE ST2
2., 2., 2., 2., 3., 0.
0., 0., 15.875, 67809192., .00000022
.00002163, 0., .00002163
-0.0, -0., 0., -0.
16., -20., -20., 16.
0.2401, 5.5917, -5.0148, 10.5408, 0., 0.
0.2401, 5.5917, -5.0148, 10.5408, 0., 0.
0., 0., 0., 0., 0., 0.
-.0, 0.
0., 0., 0., 0., 0., 0., 0.
0., 0., 0., 0., 0., 0., 0.
SHRT
.00000698, 0., 0., 0., 0.00002163, 0.
SHRT
0.014, 0., 0., 0., 0., 0.
DRIFT 31
0., 31.0,
```

```
COLD
1., 0., 0., 5., 5.
DRIFT 32
27.085, 32.0,
SHRT
0., 0., 0., 0., 0., 0.
POLES Q6
3., 3., 3.
0., 0., 25.23, 5.3975
-.05091622, 0., 0., 0., 0.0
18.89, -13.494, -13.494, 18.89
.295, 6.30221, -3.51059, .29528, 1.19866, -.423408
.295, 6.30221, -3.51059, .29528, 1.19866, -.423408
0.
SHRT
0., 0., 0., 0., 0., 0.
COLD
1., 0., 0., 5., 5.
DRIFT 33
0., 33.0,
COLD
1., 0., 0., 7.5, 7.5
DRIFT 34
25.695, 34.0,
SHRT
0., 0., 0., 0., 0., 0.
POLES Q7
3., 3., 3.
0., 0., 33.38, 7.9375
.0731129, .00, 0., 0., 0.
23.813, -19.844, -19.844, 23.813
0.225, 6.22466, -2.38148, .2341, -.72032, .72371
0.225, 6.22466, -2.38148, .2341, -.72032, .72371
0.
SHRT
0., 0., 0., 0., 0., 0.
COLD
1., 0., 0., 7.5, 7.5
DRIFT 35
15.81, 35.0,
SHRT
0., 0., 0., 0., 0., 0.
POLES S3
3., 3., 3.
0., 0., 19.9, 8.
0., .0020298, .0, .0007228, 0.
20., -20., -20., 20.
0., 0., 0., 0., 0., 0.
0., 0., 0., 0., 0., 0.
0.
SHRT
0., 0., 0., 0., 0., 0.
COLD
1., 0., 0., 7.5, 7.5
DRIFT 36
0., 36.0,
COLD 1st BCM bellows
1., 0., 0., 7.409, 7.409
DRIFT 37
9.8, 37.0,
COLD 2nd BCM bellows
1., 0., 0., 7.409, 7.409
DRIFT 38
26., 38.0,
COLD
0., 0., 0., 40., 4.5
DRIFT
9.3
SHRT
-.33216, 0., 0., 0., 0., 0.
DIPOLE D2
1., 1., 1., 1., 3., 0.
0., 0., 12., 81.3, .26520546
75., 29., 29.
-0.00, -0., 0., -0.
36., -30., -30., 36.
.3295, 3.31886, -1.2036, .181157, .1103868,
-.029513
.3295, 3.31886, -1.2036, .181157, .1103868,
-.029513
0., 0., 0., 0., 0., 0.
0., 0.
0., 0., 0., 0., 0., 0., 0.
0., 0., 0., 0., 0., 0., 0.
SHRT
.33216, 0., 0., 0., 0., 0.
COLD
0., 0., 0., 40., 4.5
DRIFT 39
0., 39.0,
DRIFT 40 mon3
56.076, 40.0,
DRIFT 41
12.05, 41.0,
```

SHRT
-0.014, 0., 0., 0., 0., 0.
DIPOLE ST3
2., 2., 2., 2., 3., 0.
0., 0., 15.875, 68603831., .00000022
.00002163, 0., .00002163
-0.0, -0., 0., -0.
16., -20., -20., 16.
0.2401, 5.5917, -5.0148, 10.5408, 0., 0.
0.2401, 5.5917, -5.0148, 10.5408, 0., 0.
0., 0., 0., 0., 0., 0.
-.0, 0.
0., 0., 0., 0., 0., 0., 0.
0., 0., 0., 0., 0., 0., 0.
SHRT
.00000698, 0., 0., 0., 0.00002163, 0.
SHRT
0.014, 0., 0., 0., 0., 0.
DRIFT 42
24.084, 42.0,
COLD
1., 0., 0., 7.5, 7.5
SHRT
0., 0., 0., 0., 0., 0.
POLES Q8
3., 3., 3.
0., 0., 33.38, 7.9375
.05420925, .00, 0., 0., 0.
23.813, -19.844, -19.844, 23.813
0.225, 6.22466, -2.38148, .2341, -.72032, .72371
0.225, 6.22466, -2.38148, .2341, -.72032, .72371
0.
SHRT
0., 0., 0., 0., 0., 0.
COLD
1., 0., 0., 7.5, 7.5
DRIFT 43
0., 43.0,
COLD
1., 0., 0., 7.5, 7.5
DRIFT 44
15.81, 44.0,
SHRT
0., 0., 0., 0., 0., 0.
POLES S4
3., 3., 3.
0., 0., 19.9, 8.0
0., .015526, 0.0, .005701, 0.
20., -20., -20., 20.
0., 0., 0., 0., 0., 0.
0., 0., 0., 0., 0., 0.
0.
SHRT
0., 0., 0., 0., 0., 0.
COLD
1., 0., 0., 7.5, 7.5
DRIFT 45
0., 45.0,
COLD 1st BCM bellows
1., 0., 0., 7.409, 7.409
DRIFT 46
15., 46.0,
COLD 2nd BCM bellows
1., 0., 0., 7.409, 7.409
DRIFT 47
26., 47.0,
DRIFT
44.1
SHRT
-.089, 0., 0., 0., 0., 0.
EDIP ED2
1., 1., 1., .6
0., 0., 10., 250., 3.77557049
35.
0., 0., 50., 0.
15.1658, -14.6504, -14.6504, 15.1658
.07901, 3.90918, -.65329, 1.91401, .22838, -.80791
.07901, 3.90918, -.65329, 1.91401, .22838, -.80791
SHRT
.089, 0., 0., 0., 0., 0.
COLD
0., 0., 0., 5., 15.
DRIFT 48
0., 48.0,
COLD 1st BCM bellows
1., 0., 0., 7.409, 7.409
DRIFT 49
42.5, 49.0,
COLD 2nd BCM bellows
1., 0., 0., 7.409, 7.409
DRIFT 50
31.55., 50.0,
DRIFT
8.

```
SHRT
-0.014, 0., 0., 0., 0., 0.
DIPOLE ST4
2., 2., 2., 2., 3., 0.
0., 0., 15.875, 68603831., .00000022
.00002163, 0., .00002163
-0.0, -0., 0., -0.
16., -20., -20., 16.
0.2401, 5.5917, -5.0148, 10.5408, 0., 0.
0.2401, 5.5917, -5.0148, 10.5408, 0., 0.
0., 0., 0., 0., 0., 0.
-.0, 0.
0., 0., 0., 0., 0., 0., 0.
0., 0., 0., 0., 0., 0., 0.
SHRT
.00000698, 0., 0., 0., 0.00002163, 0.
SHRT
0.014, 0., 0., 0., 0., 0.
COLD
1., 0., 0., 6.5, 6.5
DRIFT 51
12., 51.0,
SHRT
0., 0., 0., 0., 0., 0.
POLES Q9
3., 3., 3.
0., 0., 46.7, 7.5
-.04192126, 0., 0., 0., 0.0
20.25, -18.75, -18.75, 20.25
.2535, 5.840314, -3.40247, 1.456423, 1.44575,
-.754832
.2535, 5.840314, -3.40247, 1.456423, 1.44575,
-.754832
0.
SHRT
0., 0., 0., 0., 0., 0.
COLD
1., 0., 0., 6.5, 6.5
DRIFT 52
0., 52.0,
COLD
1., 0., 0., 6.5, 6.5
DRIFT 53
19.9, 53.0,
SHRT
0., 0., 0., 0., 0., 0.
POLES Q10
3., 3., 3.
0., 0., 46.7, 7.5
.04687356, 0., 0., 0., -.00
20.25, -18.75, -18.75, 20.25
.2535, 5.840314, -3.40247, 1.456423, 1.44575,
-.754832
.2535, 5.840314, -3.40247, 1.456423, 1.44575,
-.754832
0.
SHRT
0., 0., 0., 0., 0., 0.
COLD
1., 0., 0., 6.5, 6.5
DRIFT 54
0., 54.0,
DRIFT 55
117.6693, 55.0,
COLD
0., -.15, 0., .46, .6
DRIFT 56
0., -56.0,
SENTINEL
```